scientific reports

OPEN

Experimental optimization of disc-type generators for low-velocity hydrokinetic energy harvesting

Hongzhen Wang[1], Mingjie He[1], Gaohui Li[1], Xingwei Sun[1], Pengfei Xi[1] & Nan Shao[2]✉

The Flow-induced Motion (FIM) of elastically-supported triangular prisms is experimentally investigated, with system comparisons conducted across generators of varying rated powers, to reveal the hydrokinetic energy conversion of disc-type generators. The incoming flow (U = 0.556 m/s-1.209 m/s) covers the Reynolds number range of 48,567 ≤ Re ≤ 105,606 in TrSL3. Variable load resistances R_L (4 Ω ≤ R_L ≤31 Ω) are applied to change the total damping in the system, and the optimal damping is determined through power generation experiments. The oscillation responses and energy conversion of the system are analyzed, along with displacement time history and power spectrum of the oscillations. Through experimental studies, the disc-type generator exhibits better power generation performance compared to traditional rotational generators. The results contribute to a more comprehensive understanding on the flow-induced motion and energy conversion of the disc-type generators, and the main findings can be summed as: (1) The best branch for oscillation responses is defined as the galloping branch at a larger load resistance, the maximum amplitude ratio A^*=1.72 is observed at R_L=21 Ω with the generator rated at 300 W. (2) The energy conversion of the system varied with different generators, suggesting that there exists optimal damping for the generators. (3) The generator rated at 200 W has the best performance on energy harvesting in the tests. The maximum active power is P_{max}=21.09 W at R_L=11 Ω and U_r=8.1, corresponding to the efficiency of η_{harn} = 9.15%. The maximum energy conversion efficiency is 12.13% at R_L=11 Ω and U_r=5.2, corresponding to the active power of P_{harn}=3.94 W.

Keywords Flow-induced motion, Disc-type generators, Triangular prism, Energy conversion

The growing demand for renewable energy has intensified research into sustainable power extraction from fluid flows, particularly in low-velocity environments. Ocean currents represent a high-potential resource characterized by high energy density and predictability[1–3], offering stability advantages over intermittent sources like wave and wind energy[4]. Given these attributes, ocean current energy has garnered significant global interest due to its vast reserves and development potential. Flow-induced motion (FIM) has become promising solution for exploiting these resources, leveraging phenomena such as vortex-induced vibration (VIV), galloping, and flutter to convert kinetic energy into electricity at velocities as low as 0.25 m/s[5].

Critically, FIM-based systems demonstrate superior adaptability to low-velocity ocean currents, enabling efficient energy conversion in harvesting renewable energy. Energy conversion of FIM has emerged as a transformative approach for converting fluid energy into electricity, particularly in low-velocity fluids. To obtain higher energy, most researches on FIM energy harvesting focused on optimizing oscillator design and energy conversion mechanisms. The geometric design of cross-section is important for maximizing energy conversion efficiency by increasing oscillation amplitudes and broadening frequency bands[6,7]. Recent innovations have shifted from conventional circular cylinders to non-linear, hybrid, and adaptive cross-sections to exploit complex fluid-structure interactions, such as T-section prism[8], Pentagon prism and Cir-Tria prism[9], quasi-trapezoid cylinder[10], and square cylinder[11], D-shaped section cylinder[12–14], C-shape cylinder[15], solid and hollow bluff bodies[16], triangular prism[17,18]. D-section prisms achieve 11.75% energy efficiency at 0° angle of attack, outperforming cylinders by > 40%. Angle variation (0°-180°) triggers transitions from VIV to galloping, eliminating amplitude self-limiting at high Reynolds numbers[19]. The passive turbulence control (PTC) using angled square rods was developed to trigger synergistic vortex-induced vibration (VIV)-galloping coupling, broadening operational velocity ranges while enhancing the hydrodynamic efficiency under optimized

[1]PowerChina Huadong Engineering Corporation Limited, Hangzhou 311100, Zhejiang, China. [2]School of Water Conservancy and Hydroelectric Power, Hebei University of Engineering, Handan 056038, P R China. ✉email: shaonan@tju.edu.cn

geometric configurations[20]. Analyses of tandem piezoelectric flags in upstream wakes and experimental studies on tandem C-shape cylinder wakes via pivoted flapping mechanisms have highlighted the complexity of flow-flag interactions[21,22]. Two T-section prisms in tandem arrangements exhibit "wake galloping" under downstream wake excitation[23]. Optimized spacing (L/D = 15) and load resistance (31 Ω) increase the amplitude ratio (A^*) by 38%. The combined triangular prisms had been improved the effect on enhancing vorticity, boosting amplitude by 25% under low-stiffness conditions[24], and the experimental investigation on the oscillators with different combined sections had been conducted to validate the advantages of non-linear cross-Sect[25]. The new type for FIM of flow-induced rotation was also developed[26,27]. Comparative studies of flow-induced motion energy conversion have consistently demonstrated the superior performance of triangular prisms over alternative cross-section. Experimental and numerical investigations confirm that triangular prisms uniquely sustain non-self-limiting galloping phenomenon at low velocity (0.25–1.3 m/s)[28]. Experimental investigation and numerical simulation on FIM responses and energy conversion on different types of cylinders had been conducted[29,30], and all the results revealed that the triangular prism has the optimal performance on both FIM responses and energy conversion.

Ocean currents can generate electricity by driving impellers to rotate, converting ocean current energy into mechanical energy, and then the generator converts the mechanical energy into electrical energy. Therefore, the performance of the generator directly affects the quality and efficiency of the output electrical energy, as well as the performance and stability of FIMECS. Power Take-Off System (PTO) is the tool to convert the hydrokinetic energy to electronic energy; it mainly includes piezoelectric convertor and magnetoelectric convertor. The scholars preferred to conduct the investigations with the variable-excitation generator[31] or the linear generator[32], as shown in Fig. 1. However, the disc-type generators present a compelling solution due to the axial compactness, high torque density, and adaptability to oscillatory motion. Recent studies have explored the integration into FIM systems, revealing that electromagnetic damping significantly influences oscillation amplitude and energy conversion. Axial-flux permanent magnet (AFPM) designs minimize hydrodynamic drag in submerged systems, while disc-shaped TENGs harvest omnidirectional ultra-low-frequency vibrations (0.5 Hz), demonstrating the potential of rotary electromagnetic systems in FIM applications[33]. Magnetohydrodynamic (MHD) disc generators exemplify high-power applications, with argon plasma-driven systems yielding 10.3 kW output-ranking third globally for such technologies[34]. These advantages are tempered by challenges in impedance matching and damping control. Li et al. developed a hydrokinetic turbine-based triboelectric-electromagnetic hybrid generator that harnesses bidirectional ocean currents through planetary gear-mediated unidirectional rotation, achieving synergistic power outputs of 115 mW (TENG) and 350 mW (EMG) at ultralow frequencies[35].

However, a critical challenge remains in efficiently coupling mechanical vibrations with electromagnetic generators, particularly in systems requiring compact and durable designs. The interaction among fluid-structure interaction, generator damping matching, and system damping requires further experimental validation to maximize energy conversion efficiency.

Based on the experimental investigations, this study aims to comprehensively evaluate the oscillation responses and energy conversion performance of the Flow-Induced Motion Energy Conversion System (FIMECS) with disc-type generators of different rated powers and various load resistances. The oscillations systematically cover the VIV, VIV-galloping transition, and fully developed galloping branches, revealing the influence of hydrodynamic responses on active power and energy conversion efficiency. Key operating conditions corresponding to the maximum displacement time history, peak active power, and highest conversion efficiency are identified, providing fundamental insights into the optimal matching between structural dynamics and electrical loading. The findings are expected to support the design and optimization of high-efficiency energy harvesters for practical marine applications.

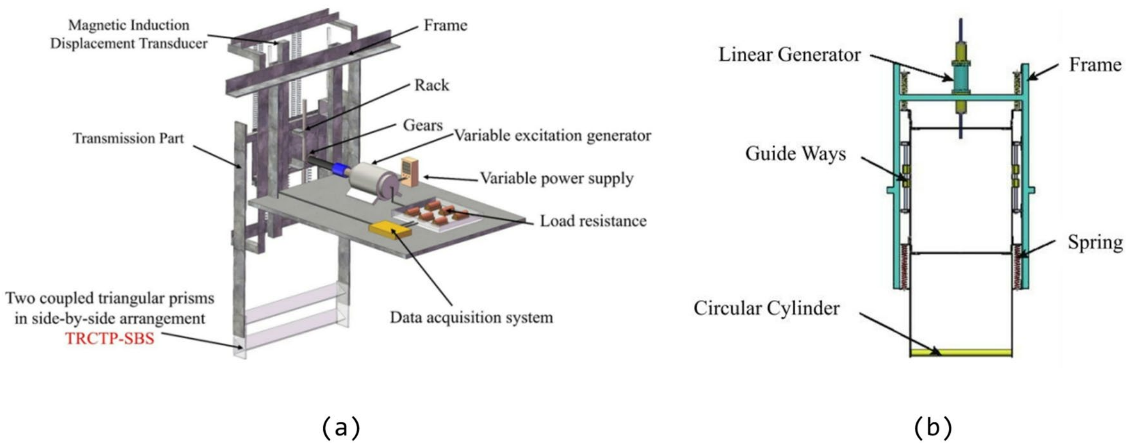

Fig. 1. Applications of generators in the energy harvesting ocean current: (**a**) Application of variable-excitation generator[31]; (**b**) Application of linear generator[32].

Experimental methods

The FIMECS mainly consists of two parts: the oscillation system and the energy conversion system in a recirculating water channel[31]. The generators applied in the tests are introduced in this section. Moreover, the free decay tests of the FIMECS with different generators are conducted and analyzed to demonstrate the physical properties of the system. The incoming flow (U = 0.556 m/s-1.209 m/s) covers the Reynolds number range of 48,567 ≤ Re ≤ 105,606 in TrSL3 (Transition in Shear Layer, 20000 ≤ Re ≤ 200000).

Physical model

Oscillation system

The oscillation system on the water channel can be moved in the direction of the coming flow. Multiple parts can be observed in the oscillation system clearly, and the main frame is made of steel. A displacement sensor was attached to the frame vertically in the 1-m wide channel to record the displacement of the oscillation system, as well as a regular triangular with a side length of 0.12 m was introduced as the cross-section of the triangular prism. The variable frequency power pump was applied to change the flow velocity, as shown in Fig. 2.

During the installation of the linear guide ways, the vertical perpendicularity deviation shall be controlled within 0.02 mm/m, and the deviation parallel to the load-bearing structure shall not exceed 0.05 mm. It is crucial to ensure that the guide ways are perpendicular to the incoming flow direction (perpendicularity error ≤ 0.5°), so as to prevent the oscillator's motion trajectory from deviating and additional friction from generating due to installation inclination.

The load-bearing steel frame is fastened to the movable trolley by high-strength bolts, with anti-slip gaskets installed between the contact surfaces. The contact area between the trolley and the flow channel of the test section must be kept flat to ensure smooth movement without jamming or deviation. After fixation, positioning pins shall be used for locking to prevent trolley displacement during the test.

The magnetic induction displacement transducer shall be strictly parallel to the linear guide ways. The connection between the sensor probe and the accessory plate of the transmission structure shall be firm and locked by special fixtures to avoid relative displacement between the probe and the accessory plate. The initial distance between the sensor probe and the measurement datum plane should be set at the mid-range position (approximately 400 mm) to prevent measurement saturation caused by approaching the two ends of the measuring range. The voltage signal lines shall adopt shielded cables and be routed away from power cables to avoid electromagnetic interference.

Energy conversion system

The Energy conversion system mainly consists of the disc-type generators and the data acquisition unit. As illustrated in Fig. 3, the disc-type generator was applied in the system to harvest energy transferred by the transmission part, and conveyed the electricity to the load resistance, simulating the consumption of electrical energy under external loads. The voltages of the resistance were recorded to reveal the energy conversion of the disc-type generators, and the data provided a foundation for following analysis.

Generators

The axial-flux, coreless permanent-magnet generators implemented in this study offer several notable advantages over conventional radial-flux DC motors: namely, higher magnetic efficiency, simplified and lightweight construction, increased power density, and reduced losses, which are conducive for energy harvesting. To investigate higher-efficiency power generation, generators with rated powers of 50 W, 100 W, 200 W, and 300 W were employed in the experiments to further enhance the energy conversion efficiency of the system, as illustrated in Fig. 4.

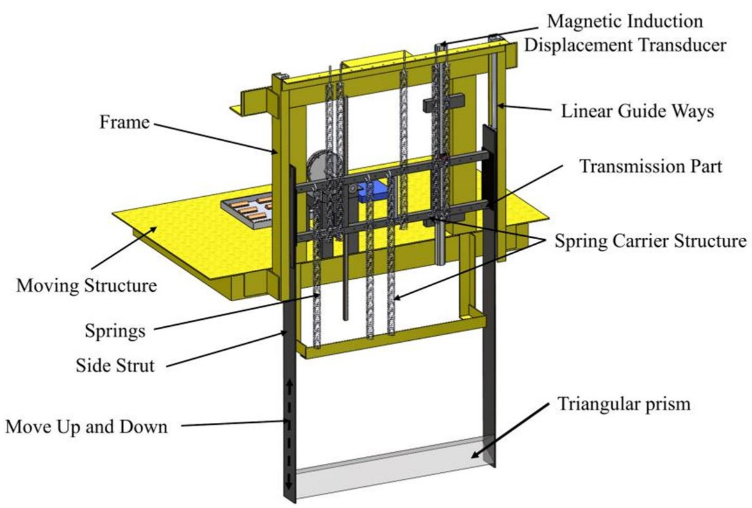

Fig. 2. Schematic diagram of oscillation system.

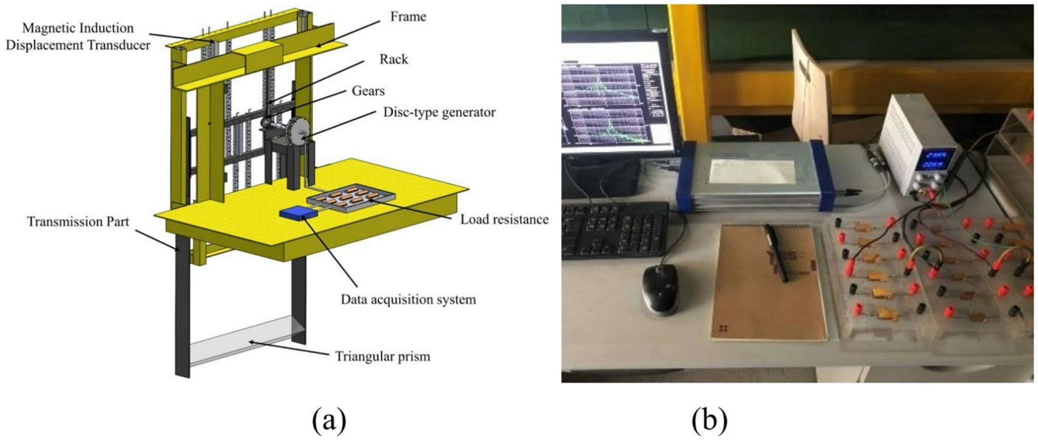

Fig. 3. Schematic diagram of energy conversion system and load resistance. (**a**) energy conversion system, (**b**) data acquisition system and load resistance.

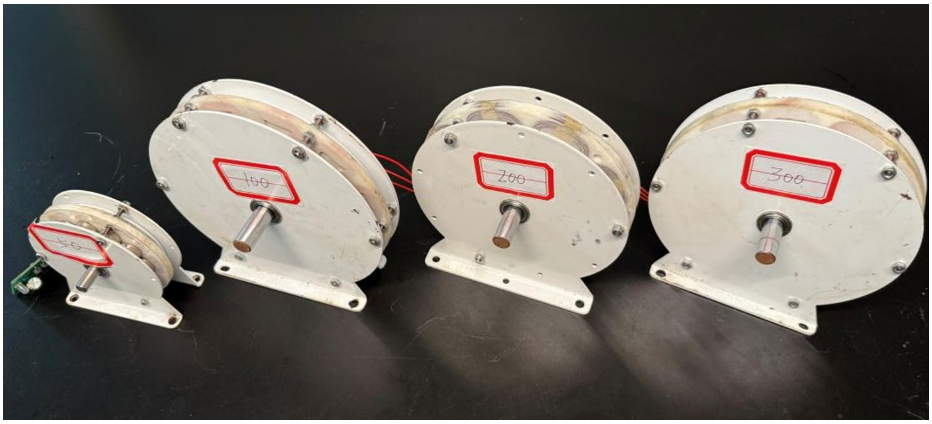

Fig. 4. Experimental generators of varying rated powers.

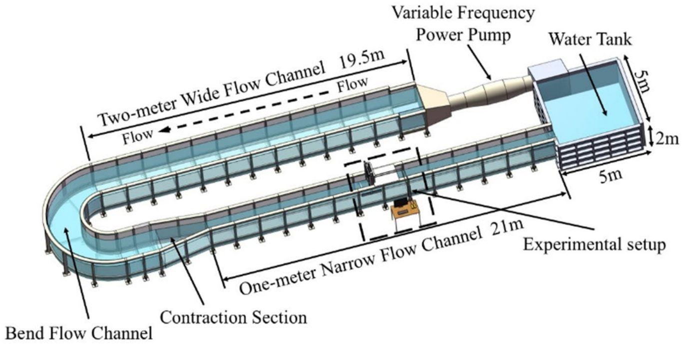

Fig. 5. Visualized self-circulating channel.

Visualized self-circulating channel

All laboratory tests in this paper were conducted in the large-scale visualized circulating flume facility of the State Key Laboratory of Hydraulic Engineering Simulation and Safety at Tianjin University.

As shown in Fig. 5, the large-scale visualized circulating flume is composed of five main components: a water storage tank, a variable-frequency power water pump, a 2-m-wide flume, a curved flume, and a 1-m-wide flume. The total length of the facility is approximately 50 m with a water storage capacity of around 200 m^3. The water storage tank has dimensions of 5 m ×5 m ×2 m. The variable-frequency power water pump has a maximum power of 90 kW, a maximum flow rate of 2600 L/s, and a maximum rotational speed of 490 r/min.

All tests were carried out in the 1-m-wide flume section, where the flow velocity could be adjusted within the range of 0–1.8 m/s. This specific flume section has a length of 21 m, a width of 1.0 m, and a depth of 1.5 m, with the water depth controlled at 1.34 m during the tests.

To ensure the accuracy of flow velocity measurements in this experiment, two sets of flow velocity testing devices, namely a Pitot tube-manometer combined velocity measuring system and a propeller-type current meter, were employed to verify the flow velocity stability.

For the Pitot tube-manometer combined velocity measuring system, the manometer has a linear measurement range of 0–6 kPa, a sensitivity of 0.1%, and an accuracy of ± 0.1%. The propeller-type current meter features a starting flow velocity of 0.01 m/s and a velocity measurement range of 0.01–4 m/s.

To analyze the variations in flow velocity and turbulence intensity of the incoming flow with water depth, the distributions of velocity and turbulence intensity were measured at water depths ranging from 15 cm to 100 cm. Owing to viscous effects, the flow velocity near the bottom tends to decrease, while the velocity difference within the experimental region (20–100 cm) is relatively small, as shown in Fig. 6(a). Turbulence intensity increases with decreasing flow velocity and increasing water depth, and the turbulence difference within the vibration region (20–100 cm) is also minimal, as presented in Fig. 6(b).

Overall, it can be ensured that the fluid acting on the oscillator within the experimental region is a uniform flow with controllable velocity.

Theoretical basis

Oscillation response of the FIMECS system

Under the action of hydrodynamic forces, the amplitude and vibration frequency of the FIM system are jointly governed by both internal and external factors of the system. Internal factors mainly include the dimensions of the oscillator and the total damping of the system, among which the factors affecting system damping consist of system stiffness, external resistance, generator selection and configuration, as well as gear-rack ratio. External factors mainly involve fluid density, fluid flow velocity, and variations in the phase difference between hydrodynamic force and the vibration displacement of the oscillator.

The dynamic equation of the FIM system can be expressed as follows:

$$A f_{osc} = \frac{\rho D l U^2 C_y \sin\phi}{4\pi C_{total}} \tag{1}$$

where A is the amplitude of the oscillator; f_{osc} is the dominant vibration frequency of the oscillator; ρ is the fluid density; D is the characteristic width of the oscillator, i.e., the projected width of the oscillator along the flow direction; l is the length of the oscillator; U is the fluid flow velocity; C_y is the maximum lift coefficient; Φ is the phase difference between vibration displacement and lift force; and C_{total} is the total damping coefficient of the system.

The system includes both mechanical damping C_{mech} and electrical damping C_{harn}, which is given by the following equation:

$$C_{total} = C_{mech} + C_{harn} \tag{2}$$

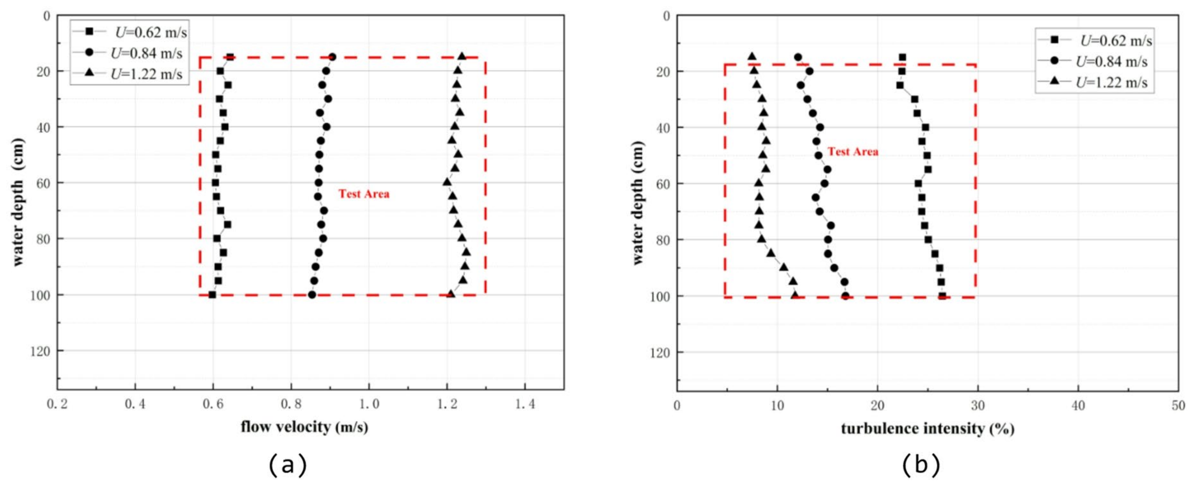

Fig. 6. Incoming flow characteristic analysis[36]. (**a**) flow velocity calibration, (**b**) turbulence intensity calibration.

where C_{mech} is the mechanical damping coefficient of the system; and C_{harn} is the electrical damping coefficient of the system.

Energy conversion of the FIMECS system
During the experiment, the electrical energy harvested by the system was dissipated in the form of resistive heat, and the voltage variation across the external resistor was collected in real time, thus enabling the calculation of the power generation capacity and energy conversion efficiency of the system.

The energy conversion efficiency is derived as:

$$\eta_{\mathrm{harn}}(\%) = \frac{P_{\mathrm{harn}}}{P_w \times BetzLimit} \times 100 \tag{3}$$

where, h_{orn} is energy conversion efficiency, *BetzLimit* is the theoretical maximum power that can be extracted from an open flow and is equal to 59.26% (16/27), P_{harn} is the active power and P_w is the total power in the fluid which is written as:

$$P_w = \frac{1}{2}\rho U^3 (2A_{max} + D)L \tag{4}$$

where, ρ is the water density, U is the incoming flow velocity, A_{max} is the maximum amplitude in the oscillation period, D is the projection width of the triangular prism in the direction of incoming flow, and L is the prism length.

Free decay test

The natural frequencies and damping ratios of the system were determined via the free decay test. To minimize the measurement error, four tests were performed per stiffness and load resistance, and the average value of the four tests was taken. The results for $K = 1600$ N/m are shown in Fig. 7.

The theoretical framework and analytical formulations governing the free decay tests have been comprehensively established in earlier studies[36–38]. The stiffness range of 1200–2000 N/m was selected to define the properties of the system and calculate the physical parameters.

Calculation formula for the natural vibration frequency of the system:

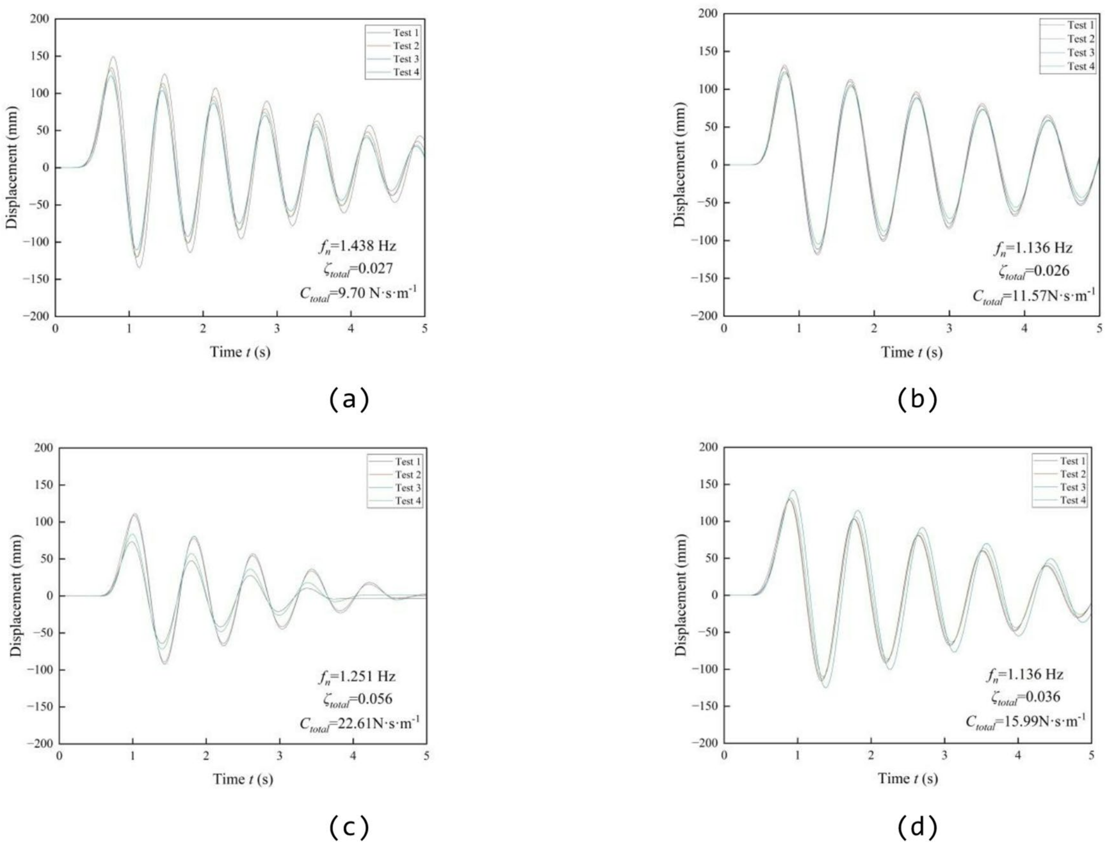

Fig. 7. Free decay tests at $K = 1600$ N/m. (**a**) Generator rated at 50 W, (**b**) Generator rated at 100 W, (**c**) Generator rated at 200 W, (**d**) Generator rated at 300 W.

K (*N*/m)	f_n (Hz)	m_{osc} (kg)	C_{total} ($N.s.m^{-1}$)	ζ_{air}
1200	1.250	19.473	9.463	0.031
1400	1.360	19.202	9.040	0.028
1600	1.438	19.622	9.703	0.027
1800	1.526	19.599	8.675	0.023
2000	1.563	20.772	10.997	0.027

Table 1. Free decay tests for generator rated at 50 W.

K (*N*/m)	f_n (Hz)	m_{osc} (kg)	C_{total} ($N.s.m^{-1}$)	ζ_{air}
1200	0.985	31.385	11.039	0.028
1400	1.069	31.073	10.801	0.026
1600	1.136	31.417	11.567	0.026
1800	1.202	31.570	10.603	0.022
2000	1.263	31.783	12.773	0.025

Table 2. Free decay tests for generator rated at 100 W.

K (*N*/m)	f_n (Hz)	m_{osc} (kg)	C_{total} ($N.s.m^{-1}$)	ζ_{air}
1200	1.078	26.188	18.599	0.052
1400	1.171	25.888	20.113	0.053
1600	1.251	25.923	22.608	0.056
1800	1.316	26.362	16.920	0.039
2000	1.389	26.289	18.685	0.041

Table 3. Free decay tests for generator rated at 200 W.

$$f_n = \frac{1}{2\pi}\sqrt{\frac{K}{m_{osc}}} \tag{5}$$

where f_n is the natural vibration frequency of the system in air, K is the system stiffness, and m_{osc} is the system mass.

Calculation formula for the system damping ratio:

$$\zeta_{air} = \frac{\ln\eta}{2\pi} = \frac{1}{2\pi}\ln(\frac{A_i}{A_{i+1}}) \tag{6}$$

where ζ_{air} is the damping ratio of the system in air; A_i is the amplitude of the i-th peak in the free decay test; A_{i+1} is the amplitude of the (i + 1)-th peak in the free decay test.

Calculation formula for the system damping:

$$\zeta_{air} = \frac{C_{mech}}{2\sqrt{m_{osc}K}} \tag{7}$$

$$C_{mech} = 2\sqrt{m_{osc}K}\cdot\zeta_{air} \tag{8}$$

Vibration parameters of the system, such as natural vibration frequency and damping ratio, are obtained via calculations using equations, (5), (6) and (7). In the free decay test, the DC motor is kept in an open-circuit state, such that only mechanical damping exists in the system. The total damping error corresponding to different stiffness values should fall within the allowable range of experimental errors (i.e., ± 5% relative to the average value). As shown in Tables 1, 2, 3 and 4, the generator rated at 50 W was abandoned due to the lowest damping, which is not conducive to high efficiency.

Results and discussion

In this section, the FIM responses and energy conversion with respect to reduced velocity (U_r) are analyzed to reveal the characteristics of the system. Considering the effects of system stiffness on the FIM responses and energy conversion of the prism, as well as the damping and natural frequency performance in Tables 1, 2, 3 and 4, the value of K = 1600 N/m was selected for the following experimental investigation. Meanwhile, to prevent

K (N/m)	f_n (Hz)	m_{osc} (kg)	C_{total} ($N.s.m^{-1}$)	ζ_{air}
1200	0.992	30.900	18.551	0.048
1400	1.069	31.073	15.496	0.037
1600	1.136	31.417	17.423	0.038
1800	1.214	30.954	14.463	0.031
2000	1.276	31.131	15.146	0.030

Table 4. Free decay tests for generator rated at 300 W.

Designation	Symbol [Unit]	Values
Width	D [m]	0.12
Length	l [m]	0.9
System stiffness	K [N/m]	1600
Range of velocity	U [m/s]	$0.556 \le U \le 1.209$
Reynolds number	$Re = \rho UD/\mu$	$48{,}567 \le Re \le 105{,}606$
Load resistance	R_L [Ω]	4,6,8,11,13,16,21,26,31

Table 5. Physical model parameters.

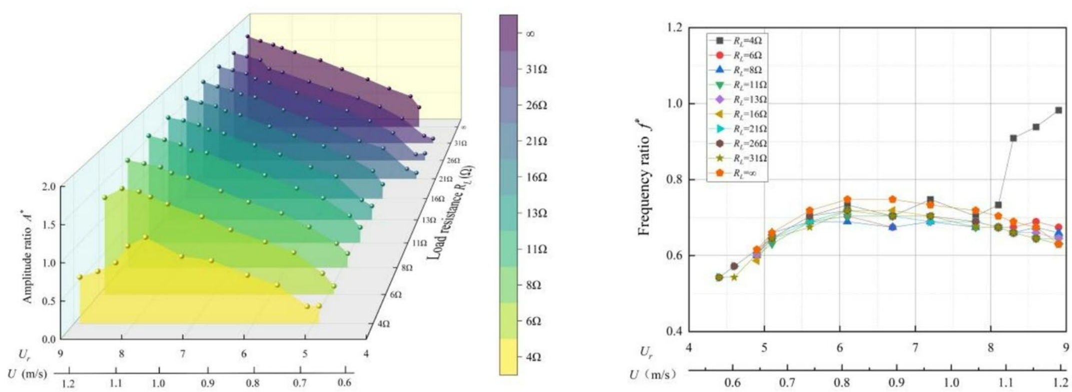

(a) (b)

Fig. 8. Oscillation response for generator rated at 100 W. (**a**) Responses of amplitude ratio, (**b**) Responses of frequency ratio.

the FIMECS and avoid the prism piercing the free surface or colliding the water channel, the parameters were controlled at reasonable range, as shown in Table 5.

Overall oscillation response

To reveal more comprehensive characteristics for the FIM responses of the triangular prism, several dimensionless parameters are defined, such as the amplitude ratio A^*, frequency ratio f^*, and reduced velocity U_r. All the analysis were based on continued oscillation at 60 s to ensure the accuracy and stability of experimental tests. As an important factor for evaluating the stability of the oscillation, the displacement time history provides valuable insights into the dynamic performance of the system. To visualize and evaluate the oscillation characteristics for different response branches, the 60 s displacement time histories with various reduced velocity for VIV and galloping are analyzed.

Generator rated at 100 W

Oscillation responses   The variation of amplitude ratio A^* and frequency ratio f^* with respect to the reduced velocity U_r at different load resistance cases are shown in Fig. 8, where a 100 W generator was employed in the system. The oscillation responses of the prism can be categorized into two distinct types: typical vortex-induced vibration (VIV) and typical galloping, and the two responses can be characterized in detail as follows:

(1) Typical VIV (R_L=4 Ω).

For R_L=4 Ω, the oscillation of the triangular prism performs as typical VIV within the tested flow velocity range of 0.67 m/s ≤ U≤1.21 m/s (4.9 ≤ U_r≤8.9), and the prism started to oscillate at U_r=4.9 (U = 0.67 m/s).

In the reduced velocity range of 4.9 ≤ U_r≤5.6, both the amplitude ratio A^* and frequency ratio f^* continued to increase with increasing U_r and performed relatively low values. Specifically, A^* increased from an initial value of 0.24 to 0.52, while f^* increased from 0.6 to 0.7, as shown in Fig. 8. The oscillation in this flow velocity range performs as the initial branch of VIV. As U_r increased to 5.6 ≤ U_r≤7.8, the oscillation performed as the upper branch of VIV. A^* increased with the increasing U_r but f^* remained at around 0.7, suggesting the appearance of the "lock-in" phenomenon with more stable oscillation. For U_r≥7.8, the A^* began to decrease, while the f^* gradually increased to approximately 0.9, indicating that the oscillation of the system entered the lower branch of VIV. As the U_r increased, the maximum frequency ratio of f^*=0.98 (U_r=8.9, U = 1.21 m/s) can be observed.

(2) Typical galloping (R_L≥6 Ω).

For the load resistance range of 6 Ω ≤ R_L≤31 Ω and the case of generator in open-circuit (R_L=∞), the oscillation of the prism performed as typical galloping. As the reduced velocity U_r continued to increase within the tested range (4.4 ≤ U_r≤8.9), the oscillation experienced the VIV initial branch, VIV-galloping branch and the fully developed galloping branch. The critical reduced velocity for starting to oscillate varied with the load resistance. Larger load resistance attributed to smaller reduced velocity (U_r=4.4) to oscillate at R_L=21 Ω, 26 Ω and 31 Ω, while the prism began to oscillate at U_r=4.9 for the remaining cases. The detailed responses can be summarized as follows:

In the reduced velocity range of 4.4 ≤ U_r≤5.6, the oscillation was in the VIV initial branch with relatively low values of both A^* and f^*. However, both the responses increased gradually with increasing U_r, which indicates the enhancement of resonance. Specifically, A^* increased from 0.1 to approximately 0.59–0.72, and f^* increased from around 0.54 to about 0.72, representing more violent and stable oscillation with increasing reduced velocity. For 5.6 ≤ U_r≤7.8, due to the combined effects of resonance and lift-force instability in the VIV-galloping branch, A^* increased significantly from 0.79 to 0.89 to 1.28–1.40, and larger load resistance attributed to higher A^*. The f^* stabilized at 0.7 and performed decreasing trend. As the U_r increased to U_r≥8.1 without suppression in the system, the oscillation entered the fully developed galloping branch. A^* continued to increase with increasing reduced velocity, reaching a maximum value of A^*=1.69 (R_L=∞), while f^* remained stable within the range of 0.65–0.70. Once galloping was established, no significant attenuation of amplitude ratio was observed during the experiments. However, due to experimental limitations, the maximum reduced velocity tested was U_r=8.9 (U = 1.21 m/s).

Displacement time history For the case of R_L=4 Ω, the oscillation entered VIV at U = 0.67 m/s (U_r=4.9). In the initial branch of VIV, the oscillation exhibited pronounced instability: the displacement time history curve performed significant fluctuations, and the overall amplitude remained at a relatively low level. As shown in Fig. 9, the maximum displacement of 47.47 mm can be observed at U = 0.67 m/s (U_r=4.9). The fluctuation in displacement became more significant at U = 0.7 m/s (U_r=5.1). However, as the flow velocity increased to U = 0.76 m/s (U_r=5.6), the fluctuations in oscillation gradually disappeared and the oscillation performed more stably with a maximum displacement of 77.92 mm.

With increasing flow velocity, the oscillation entered the upper branch of vortex-induced vibration (VIV) at U = 0.83 m/s (U_r=6.1). The increasing excitation force exerted by the fluid on the prism increased accordingly, driving a steady growth in oscillation amplitude. There were more stable oscillation and little fluctuations in the displacement time history. The maximum value of 158.84 mm can be observed at U = 1.06 m/s (U_r=7.8), as shown in Fig. 10(a). Compared with the initial branch, there were characterized by more stable oscillation performance and larger amplitudes.

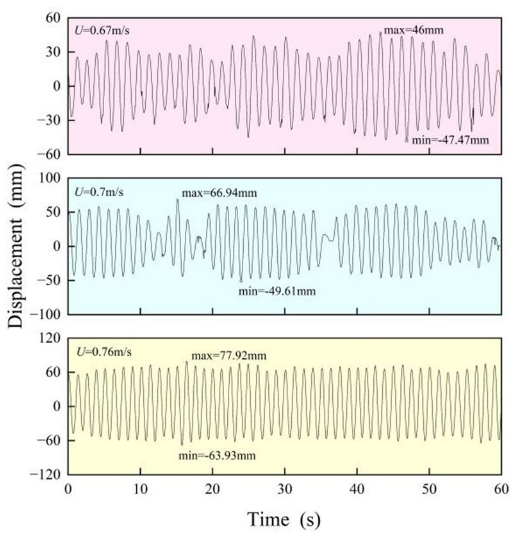

Fig. 9. Displacement time histories of VIV initial branch at R_L=4 Ω.

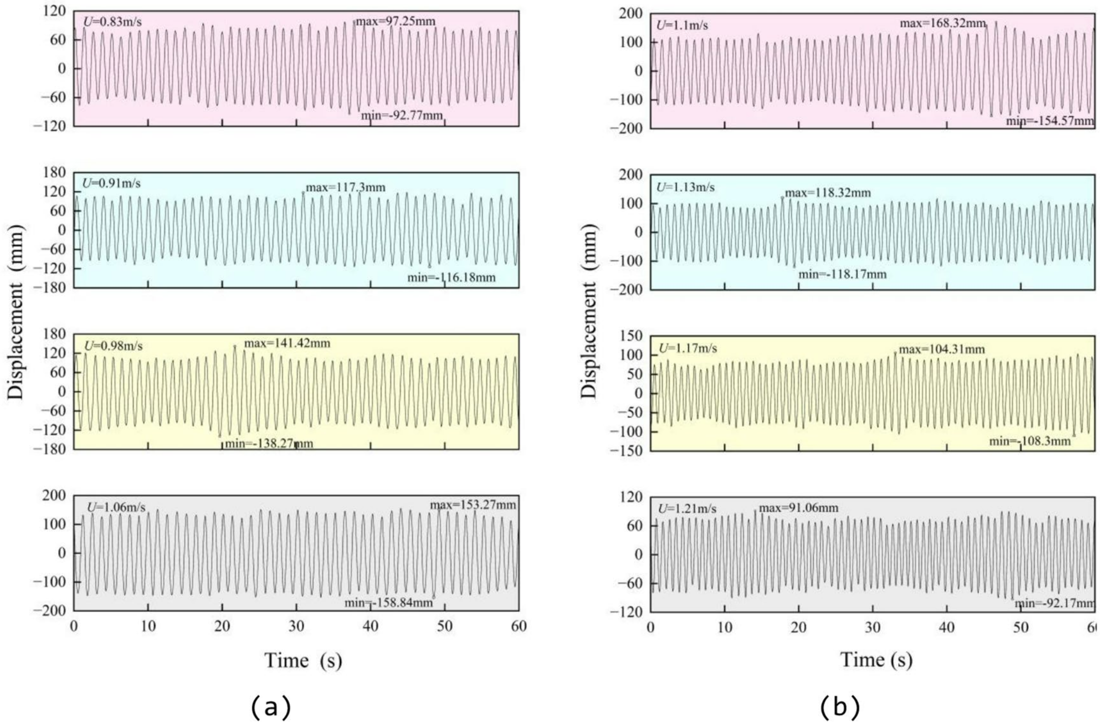

Fig. 10. Displacement time histories of VIV at R_L=4 Ω. (**a**) upper branch, (**b**) lower branch.

As the flow velocity continued to increase and reached U = 1.1 m/s (U_r=8.1), the oscillation entered the VIV lower branch, as well as the fluctuations in the displacement time history became more obvious again. For $U \geq$ 1.13 m/s ($U_r \geq$8.3), the displacement time history displayed a trend toward disorder, and the amplitude showed no evident pattern of steady growth or frequency locking in the time domain, as shown in Fig. 10(b).

For $U \geq$ 1.10 m/s ($U_r \geq$8.1) at R_L=31 Ω, the oscillation entered the galloping branch. The displacement time history performed neither pronounced amplitude jumps nor irregular fluctuations. The oscillation was characterized by large amplitudes and high stability, with the displacement values being markedly greater than those observed in all branches of VIV, as shown in Fig. 11.

<u>Frequency spectrum</u> As shown in Fig. 12, within the range of 4.9 ≤ $U_r \leq$5.6, the oscillation entered the VIV initial branch. As the reduced velocity increased, the frequency band narrowed from its initially broad distribution, indicating a progressive concentration of oscillation energy, accompanied by a slight increase in the dominant frequency toward the natural frequency. For 5.6 ≤ $U_r \leq$7.2, the oscillation transitioned into the VIV upper branch, where the frequency band became narrower and the dominant frequency was clearly defined, indicating a stable oscillation. The oscillation frequency closely matched the natural frequency, evidencing a pronounced "lock-in" phenomenon with strongly concentrated oscillation energy. As the reduced velocity increased to $U_r \geq$7.8, the frequency spectrum performed a relatively wide band with multiple peaks, the dominant frequency became indistinct, and the energy was widely dispersed, indicating a significant detuning behavior and marking the transition into the lower branch of VIV.

For the case of R_L=31 Ω, the oscillation performed as soft galloping. Within the range of 4.4 ≤ $U_r \leq$5.6, the oscillation entered the VIV initial branch with a relatively wide frequency band and poor periodicity, as shown in Fig. 13. As the flow velocity increased, the frequency band progressively narrowed, and the oscillation energy became increasingly concentrated. For 5.6 ≤ $U_r \leq$7.8, the oscillation entered the VIV-galloping branch, where the frequency band continued to narrow and the dominant frequency became more pronounced, indicating a significant improvement in oscillation stability, with the energy being relatively concentrated. As the flow velocity increased to $U_r \geq$8.1, the dominant frequency became highly distinct, the bandwidth was very narrow, and the oscillation energy was strongly concentrated. The system exhibited a relatively large oscillation intensity with a comparatively low oscillation frequency. Meanwhile, weak second-harmonic and third-harmonic components were present, which was caused by the high flow velocity and complex modes of vortex shedding. However, the harmonic energy was significantly smaller than that of the oscillation frequency, thus the overall oscillation stability was not compromised.

Generator rated at 200 W

<u>Oscillation responses</u> The variation of amplitude ratio A^* and frequency ratio f^* with respect to the reduced velocity U_r at different load resistance cases is shown in Fig. 14, where a 200 W generator was employed in the

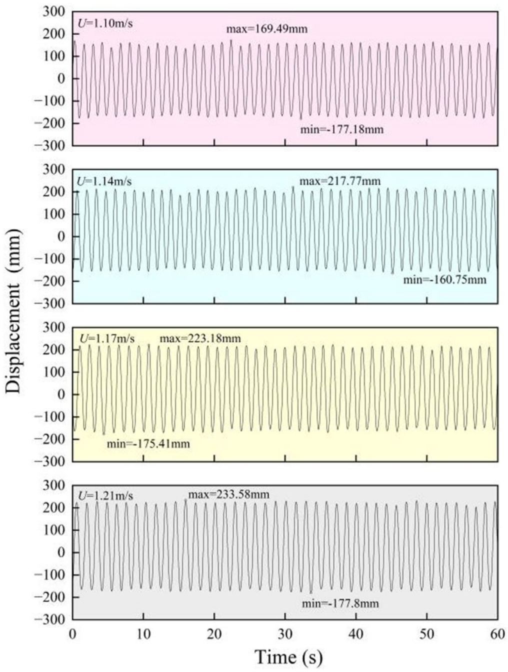

Fig. 11. Displacement time histories of galloping branch at R_L=31 Ω.

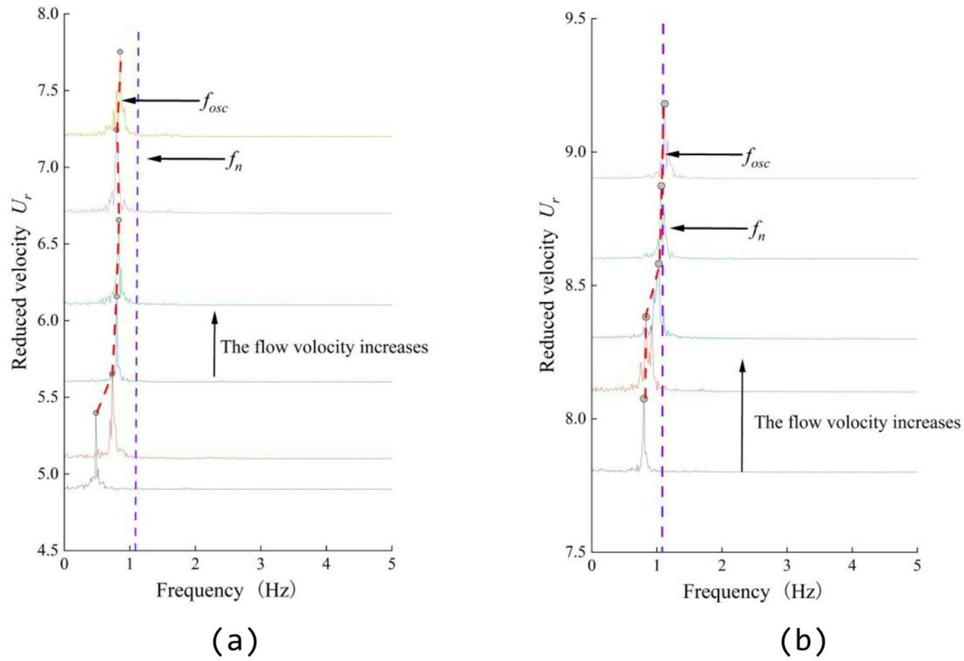

Fig. 12. Power spectrum at R_L=4 Ω. (**a**) Initial and upper branch of VIV, (**b**) Lower branch of VIV.

system. There are two significant FIM responses of VIV and galloping, and the responses can be characterized in detail as follows:

(1) Typical VIV (R_L=4 Ω, 6 Ω, 8 Ω).

Both the VIV initial branch and VIV upper branch can be observed clearly in the oscillations at R_L=4 Ω, 6 Ω and 8 Ω, and the prism started to oscillate at U_r=4.2 (U = 0.63 m/s). Within the lower reduced velocity range of $4.2 \le U_r \le 5.6$, the amplitude ratio and frequency ratio remained relatively small values. Specifically, A^* increased from an initial value of 0.13–0.19 to 0.41–0.60, while f^* rose from approximately 0.5 to around 0.7, indicating the characteristic of the VIV initial branch. As U_r increased to $5.6 \le U_r \le 8.1$, both the A^* and f^* performed significant increasing trend. The A^* increased from 0.41 to 0.60 to 0.50–0.76, and f^* increased from around 0.7 to the range

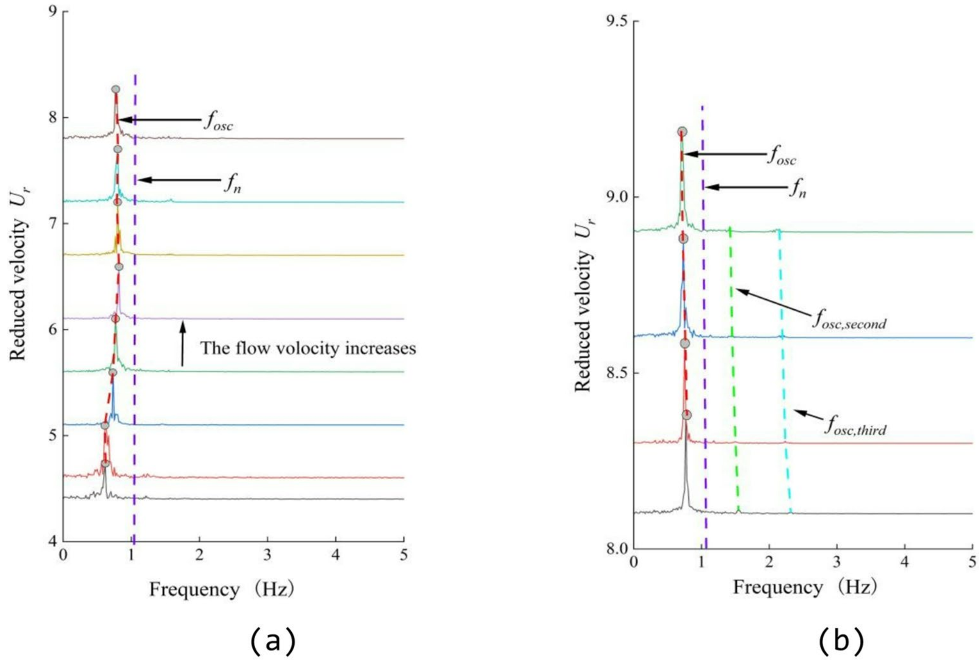

Fig. 13. Power spectrum at R_L=31 Ω. (**a**) VIV initial and VIV-galloping branch, (**b**) Galloping branch.

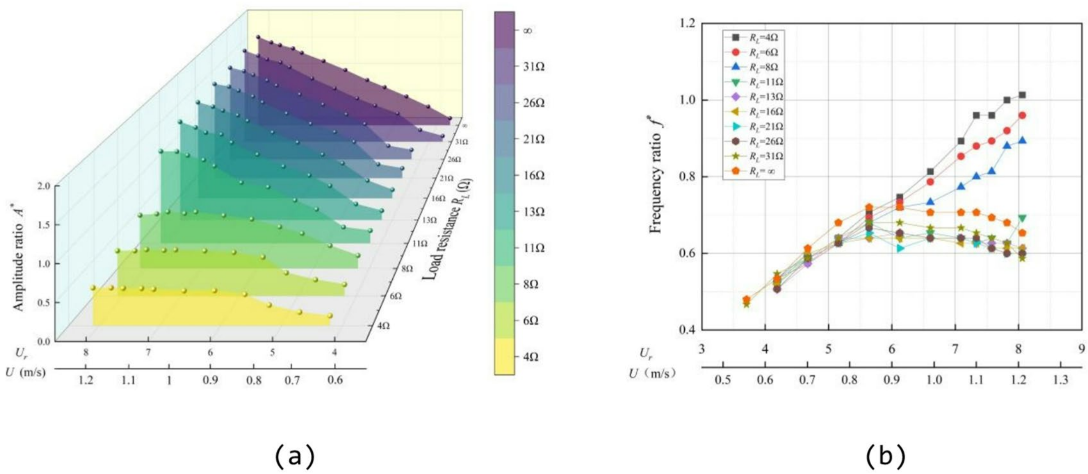

Fig. 14. Oscillation response for generator rated at 200 W. (**a**) Responses of amplitude ratio, (**b**) Responses of frequency ratio.

of 0.89–1.01. The maximum value of A^* and f^* were respectively A^*=0.76 at U_r=8.06 (R_L=8 Ω) and f^*=1.01 at U_r=8.06 (R_L=4 Ω). It was also noted that a higher load resistance generally led to larger amplitude ratios, whereas the frequency ratio tended to decrease at a constant reduced velocity.

(2) Typical galloping (R_L≥11 Ω).

For the load resistance range of 11 Ω ≤ R_L≤31 Ω and the case of generator in open-circuit (R_L=∞), the amplitude ratio A^* continued to increase as U_r increased without decreasing trend. The critical reduced velocity for the start of oscillation varied depending on the load resistance value. For R_L≥31 Ω, where the total damping of the system was relatively low, the oscillation initiated at U_r=3.7 (U = 0.56 m/s), while the system started to oscillate at U_r=4.2 (U = 0.63 m/s) for the remaining load resistance. The responses can be summarized as follows:

In the range of 3.7 ≤ U_r≤5.2, the oscillation performed as the VIV initial branch, Both the amplitude ratio A^* and frequency ratio f^* remained relatively low values but increased gradually as the flow velocity rose. The A^* increased from approximately 0.1 to 0.5–0.7, while the frequency ratio increased from about 0.5 to 0.65, reflecting enhanced resonance performance and increasing oscillation intensity. As the reduced velocity U_r increased to 5.2 ≤ U_r≤7.1, the transition from VIV to galloping was observed significantly. This phase was marked by a significant amplification in oscillation amplitude, with A^* rising from 0.5 to 0.7 to 1.15–1.33. A higher resistance typically led to a larger amplitude. Meanwhile, the frequency ratio f^* tended to decrease and stabilize around 0.6–0.7. Compared with the initial VIV branch, the VIV-galloping transition regime performed clearly improved oscillation intensity and stability. For U_r≥7.1, the oscillation entered the fully developed galloping branch. The amplitude ratio reached a maximum value of A^*=1.62 at the case of generator in open-circuit (R_L=∞), while the frequency ratio remained relatively stable within the range of 0.6–0.7. Throughout the galloping regime, the A^* kept to increase without decreasing trend. However, due to the experimental constraints, the maximum achievable U_r in the tests was limited to U_r=8.1 (U = 1.2 m/s).

Displacement time history Typical cases of R_L=4 Ω for VIV and R_L=31 Ω for galloping branches were considered to evaluate the oscillation with a generator rated at 200 W, and the displacement time histories at 60 s were analyzed.

As the reduced velocity increased to U = 0.63 m/s (U_r=4.2) at R_L=4 Ω, the oscillation entered the VIV initial branch with pronounced instability in the oscillation and strong fluctuations in the displacement time history. After approximately 40 s, larger fluctuations can be observed, although the overall amplitude remains at a low level, with the maximum absolute amplitude being 33.36 mm. As the flow velocity increased, the amplitude gradually grew, reaching a maximum value of 51.94 mm at U = 0.77 m/s (U_r=5.1), as shown in Fig. 15.

For U ≥ 0.85 m/s (U_r≥5.6) at R_L=4 Ω, the oscillation began to enter the VIV upper branch, where the fluctuations in displacement time history became relatively small and the oscillation was highly stable, as illustrated in Fig. 16. At U = 1.21 m/s (U_r=8.1) in the VIV upper branch, the maximum value of amplitude can reach 73.25 mm.

For the case of R_L=31 Ω, the oscillation entered the galloping branch at U ≥ 1.1 m/s (U_r≥7.3), with strongly stable displacement. Due to the combined effects of resonance and lift-force instability, the oscillation was characterized by extremely large amplitude and high stability. At the maximum reduced velocity in the galloping branch of U = 1.21 m/s (U_r=8.1), the peak value of the amplitude reached 209.36 mm, which is significantly greater than that in the VIV branches, as shown in Fig. 17.

Frequency spectrum As shown in Fig. 18, in the range of 4.2 ≤ U_r≤5.6 at R_L=4 Ω, the oscillation performed as the VIV initial branch. As the flow velocity increased, the oscillation bandwidth, initially relatively broad, gradually narrowed, indicating a progressive concentration of oscillation energy. This process is accompanied by the increase in the dominant frequency, which gradually approached the natural frequency of the system. For 5.6 ≤ U_r≤8.1, the oscillation entered the VIV upper branch, where the oscillation bandwidth became narrow and the dominant frequency was clearly pronounced, reflecting a more stable oscillation. The oscillation frequency was nearly identical to the natural frequency of the system, demonstrating a pronounced "lock-in" phenomenon, with oscillation energy becoming even more concentrated.

For the reduced velocity range of 3.7 ≤ U_r≤5.2 at R_L=31 Ω, the oscillation entered the VIV initial branch, characterized by a relatively broad frequency bandwidth and poor periodicity. As the flow velocity increased, the bandwidth gradually narrowed and the oscillation energy became increasingly concentrated. As the reduced velocity increased to 5.2 ≤ U_r≤7.1, the oscillation entered the VIV-galloping transition branch, where the frequency bandwidth continued to narrow and the dominant frequency became more pronounced. The overall stability of the oscillation response improved significantly, with the oscillation energy remaining relatively concentrated, as shown in Fig. 19. For U_r≥7.1, the oscillation entered the fully developed galloping branch, with large amplitudes, a distinct and dominant frequency, highly concentrated oscillation energy and a slight

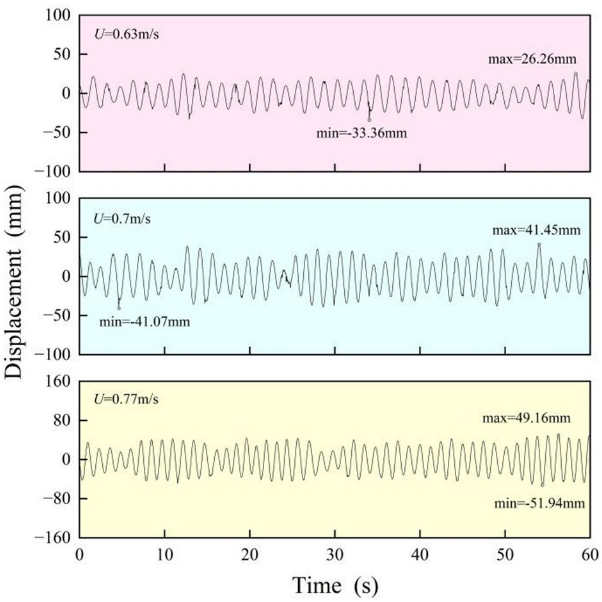

Fig. 15. Displacement time histories of VIV initial branch at R_L=4 Ω.

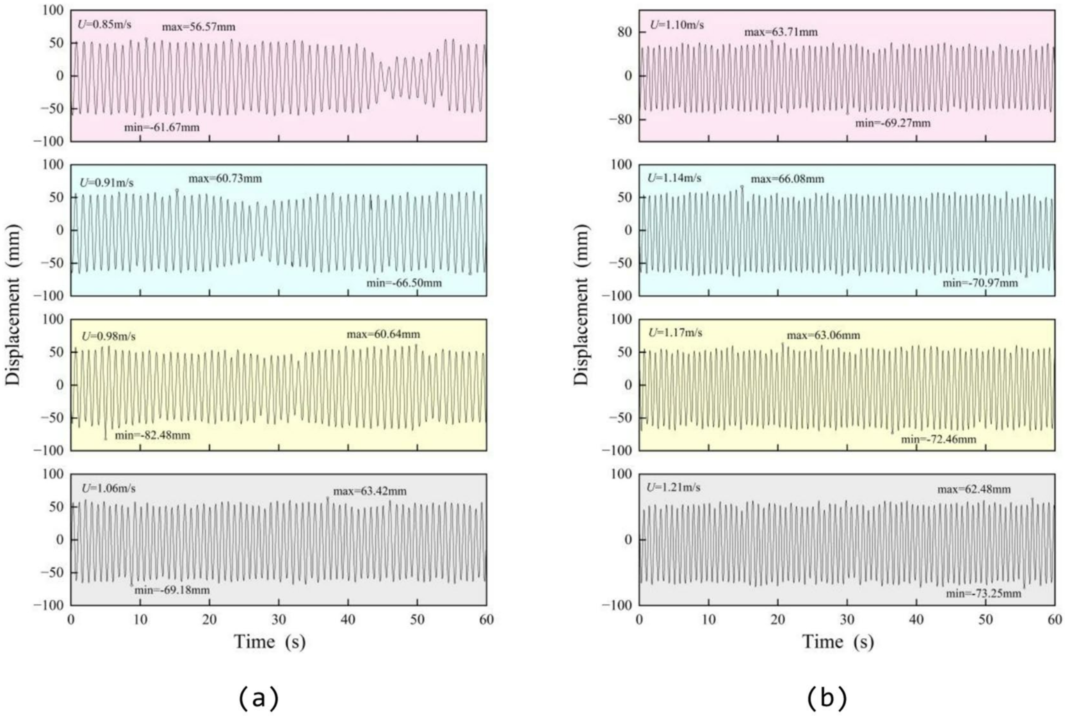

Fig. 16. Displacement time histories of VIV upper branch at R_L=4 Ω. (**a**) Cases for *U*=0.85 m/s-1.06 m/s, (**b**) Cases for *U*=1.10 m/s-1.21 m/s.

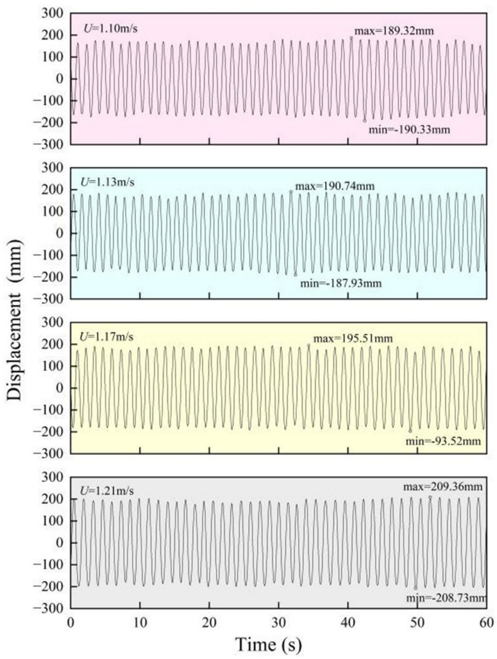

Fig. 17. Displacement time histories of galloping branch at R_L=31 Ω.

reduction in frequency value compared with the VIV-galloping transition branch. Meanwhile, weak second-harmonic and third-harmonic components were also observed, which were caused by the high flow velocity and complex modes of vortex shedding. However, the harmonic energy was significantly smaller than that of the oscillation frequency, thus the overall oscillation stability was not compromised.

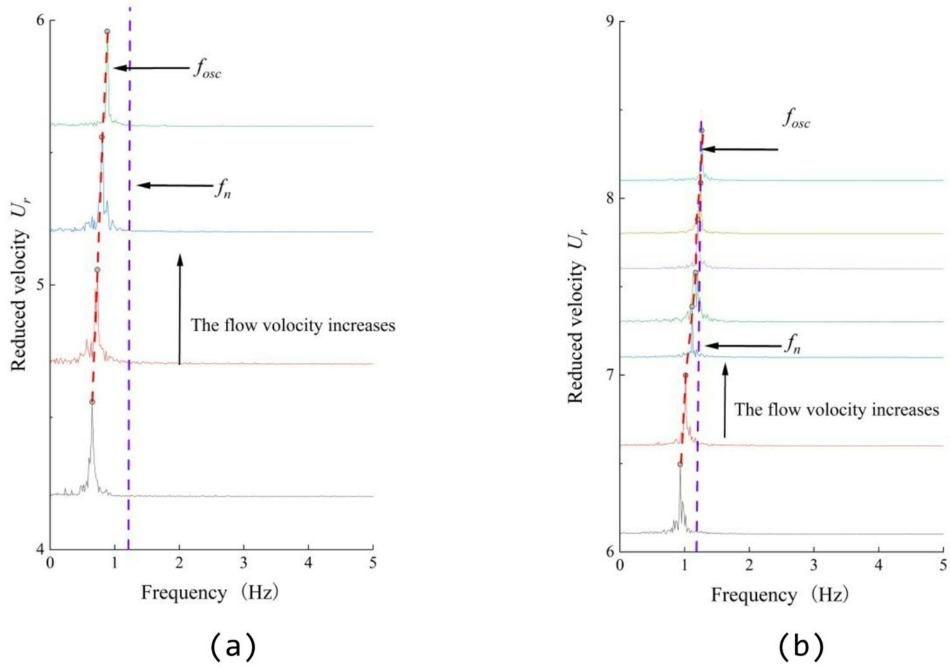

Fig. 18. Power spectrum at R_L=4 Ω. (**a**) Initial branch of VIV, (**b**) Upper branch of VIV.

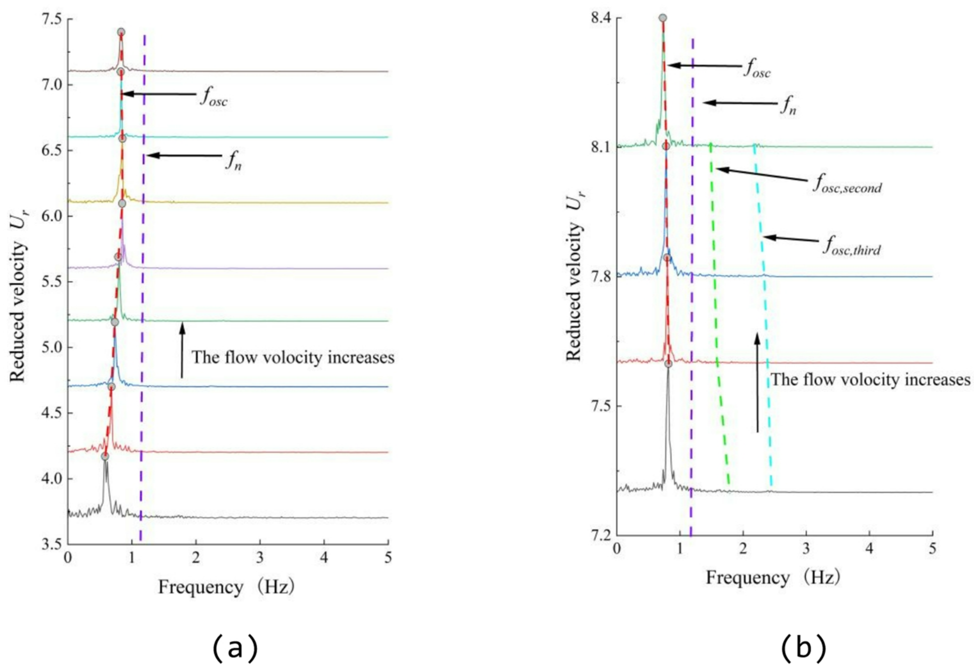

Fig. 19. Power spectrum at R_L=31 Ω. (**a**) VIV initial and VIV-galloping branch, (**b**) Galloping branch.

Generator rated at 300 W

Oscillation responses The variation of amplitude ratio A^* and frequency ratio f^* with respect to the reduced velocity U_r at different load resistance cases are shown in Fig. 20, where a 300 W generator was employed in the system. The oscillation responses of the prism performed as typical soft galloping, and the responses can be characterized in detail as follows:

For all the cases with varied load resistance of 4 Ω ≤ R_L≤31 Ω and the case of generator in open-circuit (R_L=∞), the oscillation of the prism performed as the fully developed galloping within the tested reduced velocity range of 4.4 ≤ U_r≤8.9 (0.59 m/s ≤ U≤1.21 m/s). The amplitude ratio A^* showed an overall increasing

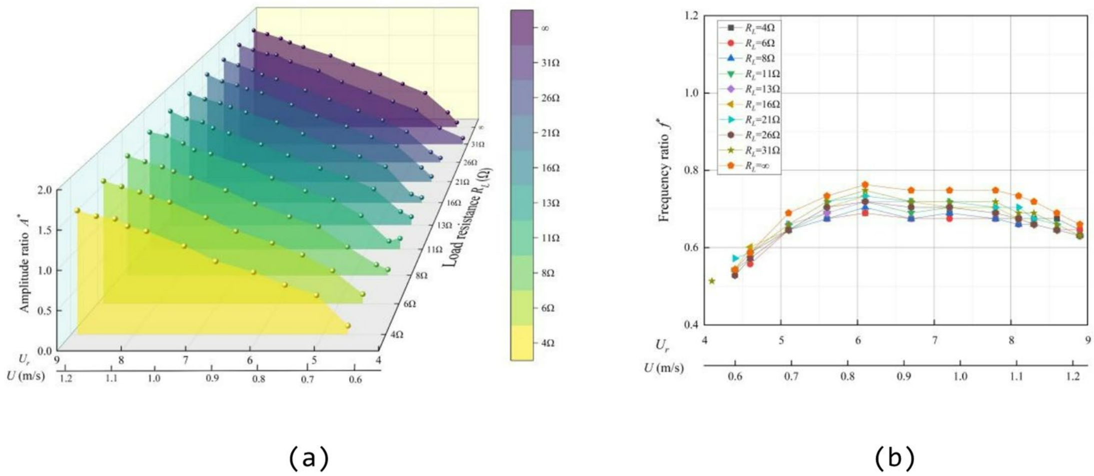

Fig. 20. Oscillation response for generator rated at 300 W. (a) Responses of amplitude ratio, (b) Responses of frequency ratio.

trend with increasing U_r, and the oscillation sequentially passed through the VIV initial branch, VIV-galloping transition branch, finally a fully developed galloping branch.

The critical reduced velocity for the start of oscillation varied depending on the load resistance value. For R_L≥8 Ω, due to the relatively lower total damping in the system, the prism started to oscillate at U_r=4.4 (U = 0.59 m/s). In contrast, for smaller load resistances of R_L=4 Ω and R_L=6 Ω, the prism started to oscillate at U_r=4.9 (U = 0.67 m/s).

In the range of 4.4 ≤ U_r≤5.6 (0.59 m/s ≤ U≤0.77 m/s), the system response was dominated by the VIV initial branch, characterized by relatively small amplitude and frequency ratios. As the reduced velocity increased, the A^* increased from approximately 0.1 to 0.63–0.77, while the f^* increased from 0.52 to 0.57 to 0.67–0.73. The gradual amplification in amplitude indicates enhanced oscillation intensity. For 5.6 ≤ U_r≤7.8 (0.77 m/s ≤ U≤1.06 m/s), the oscillation entered the VIV-galloping translation branch. Due to the combined effects of resonance and lift-force instability, the A^* increased from 0.63 to 0.77 to 1.31–1.42 sharply, and it was obvious that larger load resistance led to higher amplitude ratio. The f^* became relatively stable around 0.7. Notably, the case of R_L=6 Ω showed a slightly higher f^* values compared to other cases. Overall, the oscillation in the VIV-galloping transition branch was more stable and more intense than in the initial VIV branch. For U_r≥7.8, the oscillation entered the fully developed galloping branch. With the increasing U_r, the A^* continued to increased and reached a maximum value of A^*=1.72 at R_L=21 Ω, while the f^* remained stable around 0.65. There was no suppression existed after the oscillation entered the galloping branch, but the maximum achievable U_r in this test was limited to U_r=8.9 (U = 1.21 m/s).

Displacement time history Only soft galloping appeared with a generator rated at 300 W, thus the typical case of R_L=31 Ω for galloping branches were considered to evaluate the oscillation with a generator rated at 300 W, and the displacement time histories at 60 s were analyzed.

As the reduced velocity increased to U = 0.59 m/s (U_r=4.4), the oscillation performed as VIV initial branch. The amplitude was approximately 30 mm, with occasional local amplitude fluctuations. The oscillation presented very weak stability, as shown in Fig. 21(a). As the flow velocity increased to 0.85 ≤ U ≤ 1.06 m/s (6.1 ≤ U_r≤7.8), the oscillation entered the VIV-galloping branch. The amplitude was significantly higher than that in the initial branch although small-amplitude fluctuations remained at U = 0.85 m/s (U_r=6.1), and the waveform approached a sine shape. As the flow velocity increased, the amplitude continued to increase to 190.41 mm at U = 1.06 m/s (U_r=7.8). The fluctuations became negligible, indicating that the oscillation had entered a steady state, as shown in Fig. 21(b).

For 1.1 ≤ U ≤ 1.21 m/s (8.1 ≤ U_r≤8.9), the oscillation entered the galloping branch. The displacement time history showed no obvious amplitude jumps or fluctuations, and the oscillation remained stably within 200–220 mm, as shown in Fig. 22. The oscillation performed extremely large amplitude and high stability, with a maximum displacement of 222.14 mm, which was substantially greater than those observed in the VIV and transition branches.

Frequency spectrum As shown in Fig. 23, the oscillation of the system performed as the VIV initial branch with a relatively broad frequency band and poor periodicity at 4.4 ≤ U_r≤5.6. As the flow velocity increased, the frequency band gradually narrowed, and the oscillation energy became increasingly concentrated. For the VIV-galloping branch at 5.6 ≤ U_r≤7.8, the frequency band continued to narrow, and the dominant frequency became more pronounced, indicating a significant improvement in oscillation stability and a relatively concentrated oscillation energy. For U_r≥8.1, the oscillation entered the fully developed galloping branch, where the dominant frequency was highly prominent. The oscillation energy was highly concentrated, and the system performed strong oscillation intensity with a relatively low frequency. Meanwhile, weak second-harmonic and

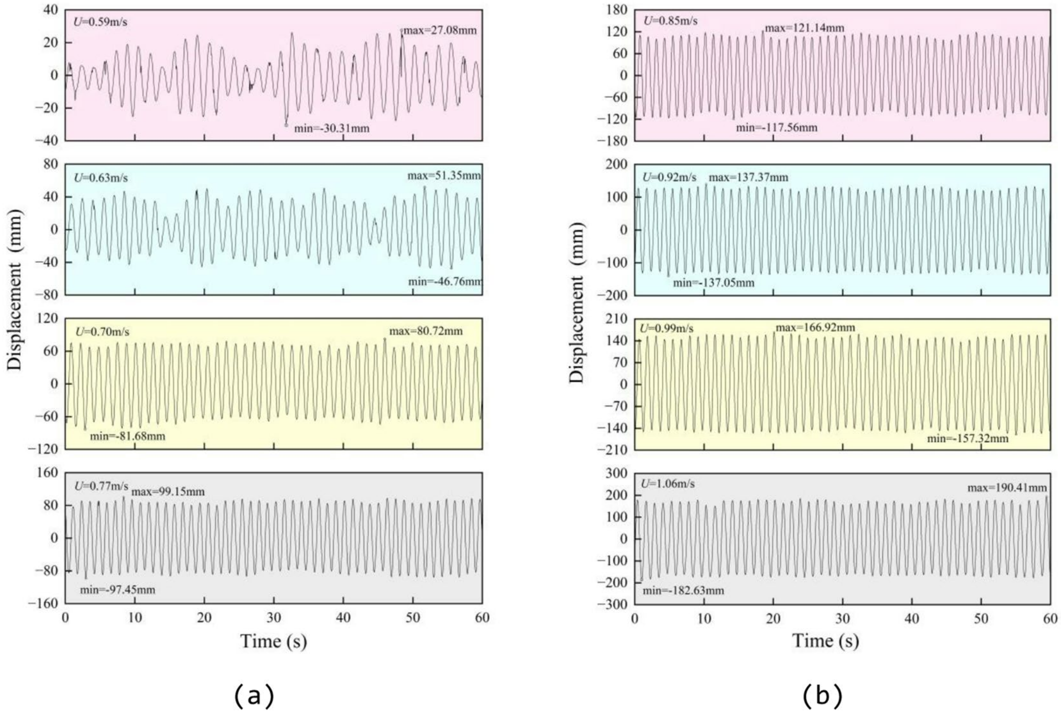

Fig. 21. Displacement time histories of VIV at R_L=31 Ω. (**a**) initial branch, (**b**) galloping branch.

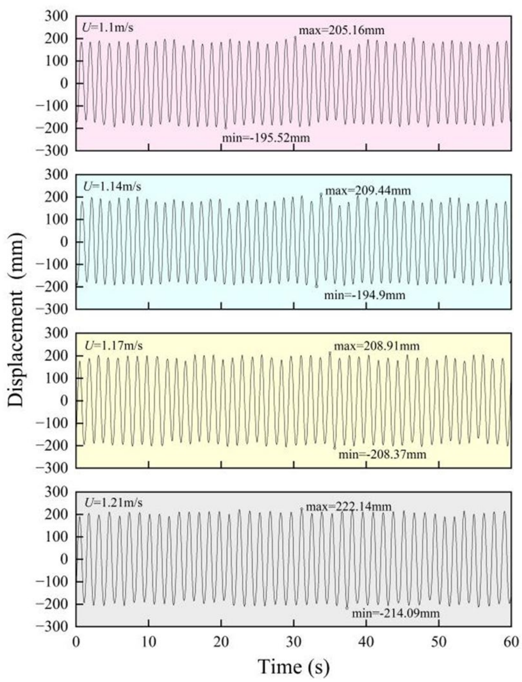

Fig. 22. Displacement time histories of galloping branch at R_L=31 Ω.

third-harmonic components were also observed, which were caused by the high flow velocity and complex modes of vortex shedding. However, the harmonic energy was significantly smaller than that of the oscillation frequency, thus the overall oscillation stability was not compromised.

Energy conversion

In this section, according to the results of energy conversion tests, the variations of the active power P_{harn} and energy conversion efficiency η_{harn} of the system with different load resistances were calculated and analyzed,

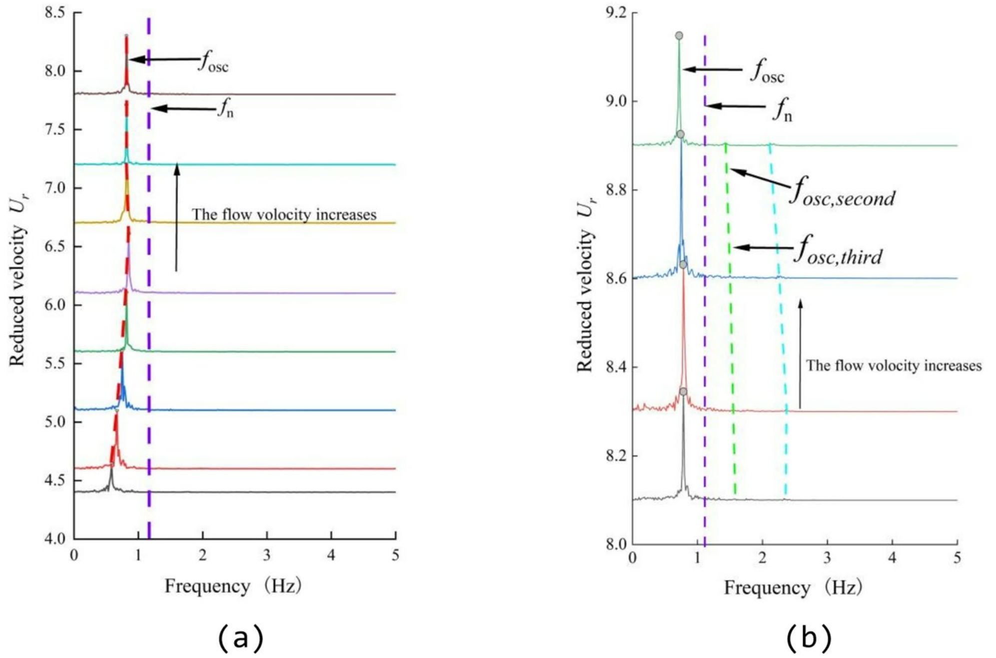

Fig. 23. Power spectrum at R_L=31 Ω. (**a**) VIV initial and VIV-galloping branch, (**b**) Galloping branch.

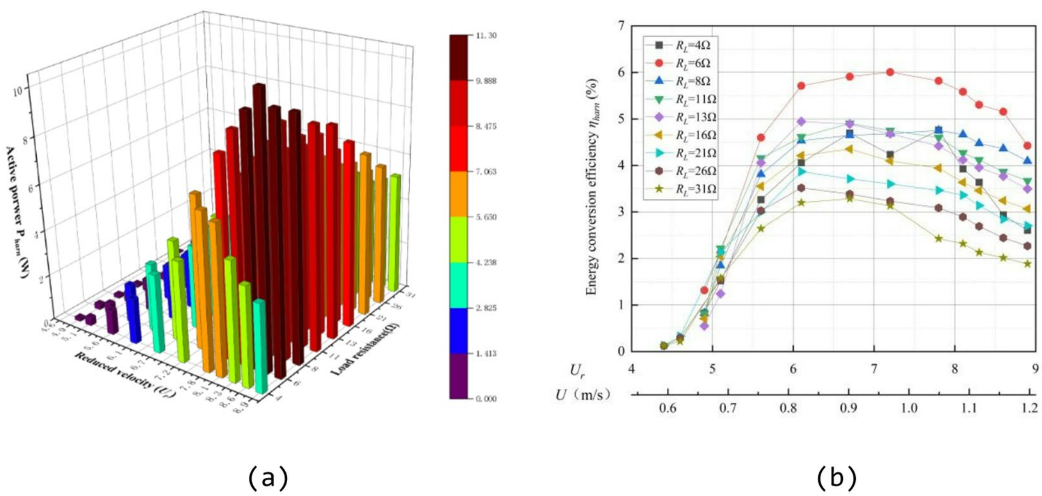

Fig. 24. Energy conversion for generator rated at 100 W. (**a**) Active power, (**b**) Energy conversion efficiency.

where P_{harn} is defined as the average value of the instantaneous power over the 60 s monitoring sample. As the reduced velocity U_r increased, the oscillation of the system performed different modes with varied load resistance, such as the VIV and galloping, which is mainly depended on the value of total damping in the system. The difference in the oscillation responses directly resulted in distinct energy conversion characteristics.

Energy conversion analysis for generator rated at 100 W

As shown in Fig. 24, the active power of the system corresponding to VIV first increases and then decreases as the reduced velocity within the tested range, which is fully consistent with the inherent characteristics of VIV. The amplitude ratio remains relatively low values, and the oscillation stability is highly sensitive to velocity variation. However, once the oscillation entered the galloping branch, due to the lift-force instability, the system oscillated in large A^* and low f^*, which is conducive to energy harvesting and more stable. As a result, the active power increased steadily with increased U_r. In the tests for the generator rated at 100 W, the maximum active power value of P_{harn}=11.28 W appeared at R_L=6 Ω and U_r=8.6. Notably, the results also reveal that the variations of P_{harn} at different load resistance presented significant differences, which is caused by the varied total damping. Moreover, the oscillation was affected, thereby impacting the energy conversion of the system. The specific performances at varied load resistance are summarized as follows:

Within the tested reduced velocity, the oscillation performed as VIV at R_L=4 Ω, and the variation of the active power closely follows the typical trend of VIV: a gradual increase with reduced velocity, reaching a peak followed by a subsequent decline. The maximum value of P_{harn}=6.69 W appeared at U_r=7.8 (U=1.06 m/s). For R_L=6 Ω within the tested U_r range of $4.9 \leq U_r \leq 8.9$ (0.67 m/s ≤ U ≤ 1.21 m/s), the oscillation performed as galloping. The active power presented a continuously increasing trend, rising to the maximum value of P_{harn}=11.28 W at U_r=8.6. However, the active power began to decrease at a slight rate as the U_r increased to U_r=8.9, which may be caused by the local disorder of vortex shedding. However, due to that the galloping is "self-excited", such disturbances are effectively resisted, resulting in only a marginal decrease in active power that remains near the peak value.

For the remaining cases with different resistance, similar trends were observed with the system entering the galloping branch at higher U_r. The P_{harn} increased monotonically with increasing U_r, and lower value of load resistance led to higher active power. The maximum value of P_{harn}=10.12 W appeared at R_L=8 Ω (U_r=8.9).

For the VIV branches at R_L=4 Ω, the energy conversion efficiency η_{harn} performed the trend of initial increase, followed by fluctuations and eventual decline with increasing U_r. The peak value of η_{harn} reached 4.76% at U_r=7.8. For the galloping branches at other cases, the value of η_{harn} increased with decreasing R_L. The maximum value of η_{harn} = 6% appeared at R_L=6 Ω and U_r=7.2.

Within the range of $4.4 \leq U_r \leq 5.6$, the η_{harn} increased sharply to 3%-5% as U_r increased, corresponding to the VIV initial branch. As U_r increased to $5.6 \leq U_r \leq 7.8$, the difference of η_{harn} at different load resistance became more significant. Notably, the case of R_L=6 Ω had better performance at the energy conversion efficiency with $\eta_{harn} \geq 5\%$, as shown in Fig. 24(b). For $U_r \geq 7.8$, the oscillation entered the fully developed galloping branch with larger amplitude ratios. However, the scanning area increased, resulting in a decrease in energy conversion efficiency.

As shown in Fig. 24, the results showed that there exists a optimal damping case of R_L=6 Ω with higher η_{harn}, and the maximum value of η_{harn} is 5.16% at U_r=8.6, corresponding to the active power of P_{harn}=11.28 W.

Energy conversion analysis for generator rated at 200 W

At the reduced velocity of $U_r \geq 3.7$ ($U \geq 0.56$ m/s), the system began to oscillate and generate electrical power. As the U_r increased, the oscillations performed different modes, which led to markedly different energy conversion characteristics. As shown in Fig. 25, for the cases dominated by VIV (R_L=4 Ω, 6 Ω, and 8 Ω), the active power P_{harn} generally increased with the increasing reduced velocity, indicating the VIV initial branch and the VIV upper branch. The VIV lower branch was not observed within the tested range of reduced velocity, which ensured the increase in the active power.

For the other load resistance values, the oscillation entered the galloping branch with the increasing U_r, suggesting better performance in amplitude and energy conversion. Consequently, the active power increased steadily with U_r. In the experimental tests with the generator rated at 200 W, the maximum active power value of P_{harn}=21.09 W appeared at R_L=11 Ω and U_r=8.1. The differences in the active power at different load resistance performed significantly, which was caused by the variation of total damping in the system. The active power at different load resistances can be divided into two main patterns:

(1) For the case of R_L=4 Ω, 6 Ω and 8 Ω, the oscillation of the system performed as the VIV initial branch and VIV upper branch. The variation of P_{harn} was strongly tied to the evolution of VIV: the P_{harn} increased gradually with U_r, reaching a peak value of P_{harn}=11.43 W at R_L=8 Ω and U_r=8.1.

(2) In the range of 11 Ω ≤ R_L ≤ 31 Ω, the oscillation performed as typical soft galloping within the reduced velocity range of $3.7 \leq U_r \leq 8.1$. The active power P_{harn} increased steadily, and lower resistances led to higher power at a constant U_r. In this regime, increased U_r accelerated the oscillation of the system, due to the combined effects of resonance and lift-force instability, the active power was improved. The maximum value of P_{harn}=21.09 W appeared at R_L=11 Ω and U_r=8.1.

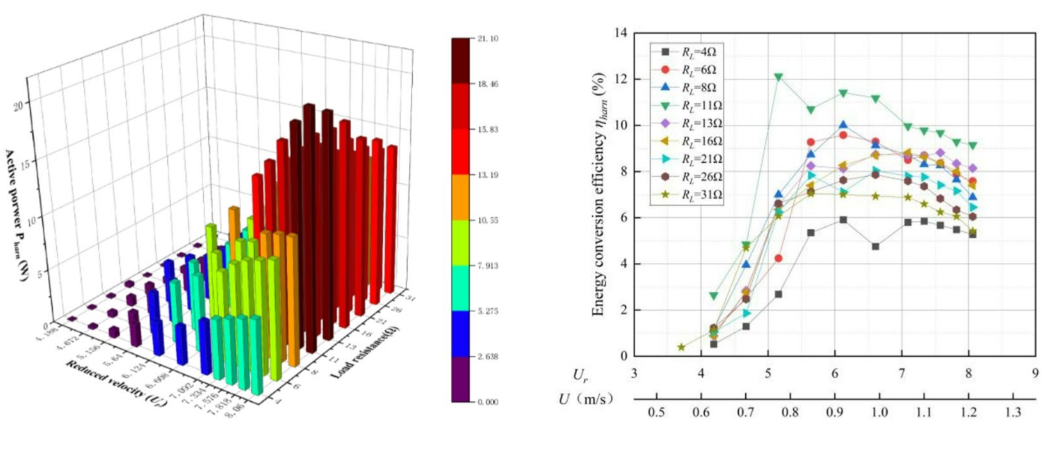

(a) (b)

Fig. 25. Energy conversion for generator rated at 200 W. (**a**) Active power, (**b**) Energy conversion efficiency.

As shown in Fig. 25(b), the energy conversion efficiency η_{harn} of the system performed a gradual increase with reduced velocity, followed by fluctuations and eventually a decline trend in the VIV regime. The peak value of η_{harn} was 10% at R_L=8 Ω and U_r=6.1. The η_{harn} presented the trend of first increase and them began to decrease after the oscillation entered the galloping branch, and the η_{harn} increased with decreasing R_L. The maximum value of 12.13% appeared at R_L=11 Ω and U_r=5.2.

In the range of $3.7 \le U_r \le 4.7$, all the η_{harn} at different load resistance presented low values due to the small fluid force, and the increasing rate was also small, corresponding to the VIV initial branch. As the U_r increased to $4.7 \le U_r \le 6.1$, the divergence in efficiency growth among the cases emerged. The case of R_L=11 Ω showed the most pronounced growth rate, reaching the maximum efficiency of η_{harn} = 12.13% at U_r=5.2. In contrast, the growth rates for other resistances were more modest, all remaining below 10%, indicating that the case of R_L=11 Ω had the best performance on energy conversion. For $U_r \ge 6.1$, the oscillation entered the fully developed galloping branch with stable amplitude ratio, but the η_{harn} began to decrease due to the increasing scanning area. The peak value of η_{harn} at the galloping branch was η_{harn} = 9.15% at R_L=11 Ω and U_r=8.1, corresponding to the active power of P_{max}=21.09 W.

Energy conversion analysis for generator rated at 300 W

As shown in Fig. 26, for the cases of different load resistance with a generator rated at 300 W in the system, the active power P_{harn} varied obviously with increasing U_r. Overall, the P_{harn} increased monotonically as U_r increased, primarily because the oscillation sequentially experienced the VIV initial branch, VIV-galloping branch and the galloping branch, which ensure the increase in amplitude and energy conversion. In the galloping branch, due to the combined effects of resonance and lift-force instability, increased amplitude resulted in larger P_{harn}. The maximum value of P_{harn}=14.01 W appeared at R_L=6 Ω and U_r=8.9 of the galloping branch. Noticeable differences were observed in the active power at different load resistance, owing to the fact that the load resistance affected the total damping in the system, thereby affecting energy conversion efficiency.

Specifically, for $4\ \Omega \le R_L \le 31\ \Omega$, the oscillation entered the galloping branch by self-excitation within the tested U_r range. In the VIV initial branch of $4.4 \le U_r \le 5.6$, due to the low amplitude, the increasing rate of P_{harn} also performed lower values. However, as the U_r increased to $5.6 \le U_r \le 7.8$ of the VIV-galloping branch, the oscillation frequency approached the natural frequency of the system, leading to a significant amplitude increase and the fastest increasing rate of active power. For $U_r \ge 7.8$, the oscillation performed as the galloping branch, where the amplitude continued to increase and the frequency locked in, resulting in further increased active power but a slower rate. The case of R_L=6 Ω had the best performance on energy conversion, and the maximum value of P_{harn}=14.01 W appeared at R_L=6 Ω and U_r=8.9.

The energy conversion efficiency η_{harn} performed the trend of rapid increase firstly with increasing reduced velocity, followed by fluctuations, and eventually a decline. The maximum value of η_{max} = 7.17% appeared at R_L=6 Ω and U_r=7.2, as shown in Fig. 26(b).

In the range of $4.4 \le U_r \le 5.6$, corresponding to the VIV initial branch, the efficiency for all the cases rapidly increased to approximately 3.5-6%. As the U_r increased to $5.6 \le U_r \le 7.8$, the efficiencies began to diverge among cases with different load resistances, where the case of R_L=6 Ω demonstrated the most pronounced increasing rate and reached the maximum energy conversion efficiency of η_{max} = 7.17% at U_r=7.2. In contrast, other cases performed slower increasing rate and even the decrease trend, which suggested that the case of R_L=6 Ω had the best performance on energy conversion. For $U_r \ge 7.8$, the oscillation entered the fully developed galloping branch, and all the η_{harn} values began to decrease, which is caused by the increasing scanning areas.

Power generation characteristics of disc generators with different rated powers

This section presents an analysis of the power generation performance of disc generators with different rated powers through experiments. It comprehensively and systematically investigates the variation law of the system

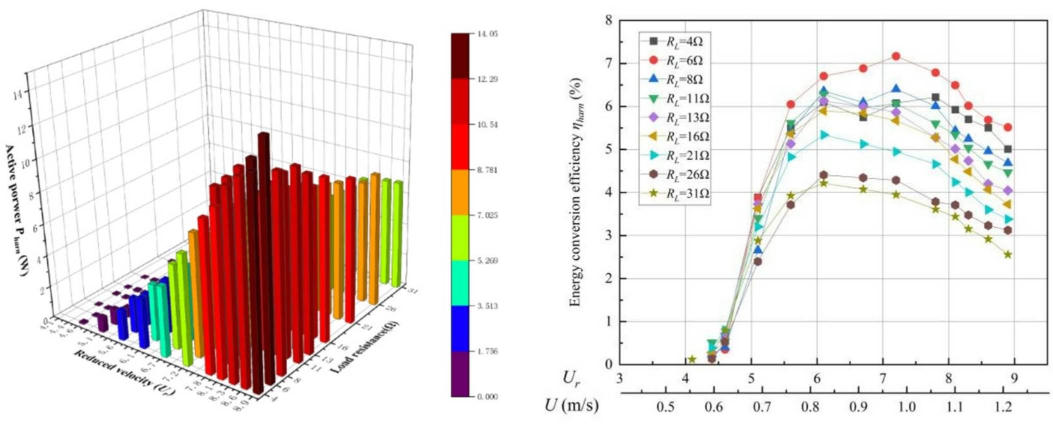

(a) (b)

Fig. 26. Energy conversion for generator rated at 300 W. (**a**) Active power, (**b**) Energy conversion efficiency.

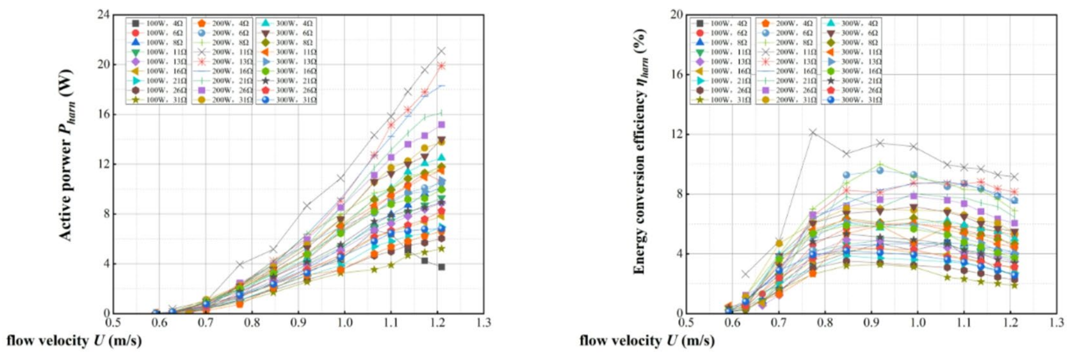

(a) (b)

Fig. 27. Overall Variation Law of Power Generation Characteristics of Disc Generators with Different Rated Powers. (**a**) Active power, (**b**) Energy conversion efficiency.

input power generation P_{harn} of motors with different powers with the actual flow velocity U under different external resistance conditions, as illustrated in Fig. 27. Herein, P_{harn} refers to the average power over a 60 s period. As the flow velocity increases gradually, the vibration system starts to output electrical energy. However, with the continuous rise of flow velocity, the oscillator exhibits different vibration modes under different external resistances R_L. Specifically, the power generation and efficiency of motors with different powers demonstrate significant differences with the change of flow velocity under varied resistance conditions. In the power generation test of the single-drive motor, the maximum power generation P_{harn}=21.09 W is achieved at the galloping branch of the triangular prism oscillator with a flow velocity U = 1.21 m/s under the condition of a 200 W single-disc generator with an external resistance R_L=11 Ω.

When R_L=4 Ω, the 100 W motor system exhibited complete vortex-induced vibration (VIV). Both the power generation output and efficiency increased first to a peak value and then decreased with the rise of flow velocity. In contrast, the 300 W motor system presented soft galloping behavior, where the power generation output increased monotonically with increasing flow velocity, reaching a maximum value of 12.50 W; its power generation efficiency increased initially and then declined, with the peak efficiency of η_{harn} = 6.22% observed at a flow velocity of U = 1.06 m/s. As for the 200 W motor system, it underwent the initial branch and upper branch of VIV successively with the increase of flow velocity. Its power generation output increased monotonically with a relatively slow growth rate, while the power generation efficiency showed a trend of rising first and then falling.

When R_L=11 Ω, all the 100 W, 200 W, and 300 W motor systems manifested soft galloping characteristics. The power generation output and efficiency of the three motor systems all exhibited an upward trend with increasing flow velocity. In the low flow velocity range (0.59 m/s ≤ U≤0.7 m/s), the power generation output of all motors remained at a low level. In the medium-to-high flow velocity range (0.7 m/s ≤ U≤1.06 m/s), the 200 W motor system achieved the fastest growth rate of power generation output. The power generation efficiency of the three motors all increased first and then decreased, with the maximum efficiency of η_{harn} = 12.13% obtained under the condition of a 200 W single-disc generator at U = 1.06 m/s in the single-drive test with R_L=11 Ω. In the high flow velocity range (1.06 m/s ≤ U≤1.21 m/s), the power generation output of the three motors continued to rise, and the maximum power generation output of 21.09 W under R_L=11 Ω was achieved by the 200 W motor system at U = 1.21 m/s.

When R_L=31 Ω, the 100 W, 200 W, and 300 W motor systems all demonstrated soft galloping behavior. The power generation output of the three motor systems increased with increasing flow velocity, while their power generation efficiency showed a trend of increasing first and then decreasing. In the single-drive test with R_L=31 Ω, the maximum power generation output of 13.77 W was achieved by the 200 W single-disc generator at U = 1.21 m/s, and the maximum efficiency of η_{harn} = 7.04% was obtained by the same 200 W single-disc generator at U = 0.85 m/s.

Conclusions

The FIM responses and the energy conversion of the FIMECS with a triangular prism were investigated experimentally. The flow velocity range of U = 0.556 m/s-1.209 m/s were selected, as well as the effects of load resistance was analyzed with different disc-type generators. The amplitude ratio A^*, frequency ratio f^*, displacement time history and the power spectrum for the oscillation are presented and discussed to reveal the performances of the system, the specific conclusions can be summarized as follows:

(1) As the reduced velocity increased, the sequential transitions from the VIV initial branch to the VIV-galloping transition branch and finally to the fully developed galloping branch can be observed in the tests. Lower total damping (higher load resistance) reduced the critical reduced velocity for oscillation onset, promoting a larger flow velocity range for oscillation.

(2) The oscillation performed low values for A^* and f^*, in the VIV initial branch, while the rapid increase in the VIV-galloping transition branch. For the fully developed galloping branch, there are always large values

with strongly stable oscillation. The maximum observed amplitude was 209.36 mm for the 200 W generator at U = 1.21 m/s (U_r=8.1) and R_L=31 Ω.

(3) The transition from VIV to galloping was consistently accompanied by a decrease in frequency ratio f^* and increase in amplitude ratio A^*, which ensured a stable oscillation and improved energy conversion performance.

(4) A systematic comparison was conducted on disc generators with different rated powers in the experiment. With the generator rated at 200 W, the preferred performance on energy conversion was achieved. The maximum active power in the tests reached P_{max}=21.09 W at R_L=11 Ω and U_r=8.1, corresponding to the efficiency of η_{harn} = 9.15%. Meanwhile, the highest energy conversion efficiency η_{harn} = 12.13% appeared at R_L=11 Ω and U_r=5.2, corresponding to the active power of P_{harn}=3.94 W.

Data availability

The data supporting the findings of this study are available from the corresponding author upon reasonable request.

Received: 24 November 2025; Accepted: 28 January 2026
Published online: 07 February 2026

References

1. Neshat, M. et al. Layout optimisation of offshore wave energy converters using a novel multi-swarm cooperative algorithm with Backtracking strategy: a case study from Coasts of Australia. *Energy* **239**, 122463 (2022).
2. Wang, J., Su, Z., Li, H., Ding, L. & Zhu, H. Gaidai, O. Imposing a wake effect to improve clean marine energy harvesting by flow-induced vibrations. *Ocean Eng.* **208**, 107455 (2020).
3. Narendran, K., Murali, K. & Sundar, V. Investigations into the efficiency of vortex- induced vibration hydro-kinetic energy device. *Energy* **109**, 224–235 (2016).
4. Rostami, A. B. & Armandei, M. Renewable energy harvesting by vortex-induced motions: review and benchmarking of technologies. *Renew. Sustain. Energy Rev.* **70**, 193–214 (2017).
5. Bernitsas, M. M., Raghavan, K., Ben-Simon, Y. & Garcia, E. Vivace (vortex induced vibration aquatic clean energy): a new concept in generation of clean and renewable energy from fluid flow. *J. Offshore Mech. Arct. Eng.* **130**, 10–24 (2008).
6. Latif, U., Dowell, H. E., Uddin, E. & Younis, M. Y. Parametric aerodynamic and aeroelastic study of a deformable flag-based energy harvester for powering low energy devices. *Energy. Conv. Manag.* **280**, 116846 (2023).
7. Latif, U., Dowell, H. E., Uddin, E., Younis, M. Y. & Frisch, H. M. Comparative analysis of flag based energy harvester undergoing extraneous induced excitation. *Energy* **295**, 130995 (2024).
8. Shao, N. et al. Experimental investigation of f low-induced motion and energy conversion of a T-section Prism. *Energies* **11** (8), 2035 (2018).
9. Zhang, B., Song, B., Mao, Z., Tian, W. & Li, B. Numerical investigation on VIV energy harvesting of bluff bodies with different cross sections in tandem arrangement. *Energy* **133**, 723–736 (2017).
10. Ding, L., Zhang, L., Wu, C., Mao, X. & Jiang, D. Flow-induced motion and energy harvesting of bluff bodies with different cross-sections. *Energy. Conv. Manag.* **91**, 416–426 (2015).
11. Zhang, M. et al. Predefined angle of attack and corner shape effects on the effectiveness of square-shaped galloping energy harvesters. *Appl. Energy*. **302**, 117522 (2021).
12. Sharma, G., Garg, H. & Bhardwaj, R. Flow-induced vibrations of elastically-mounted C- and D-section cylinders. *J. Fluids Struct.* **109**, 103501 (2022).
13. Zhao, J., Hourigan, K. & Thompson, M. C. Flow-induced vibration of D-section cylinders: an afterbody is not essential for vortex-induced vibration. *J. Fluid Mech.* **851**, 317–343 (2018).
14. Chen, W., Zhao, Y., Ji, C., Srinil, N. & Song, L. Experimental observation of multiple responses of an oscillating D-section Prism. *Phys. Fluids*. **33**, 091701 (2021).
15. Latif, U. et al. Experimental electro-hydrodynamic investigation of flag-based energy harvesting in the wake of inverted C-shape cylinder. *Energy* **215** (PB), 119195 (2021).
16. Latif, U. et al. Impact of solid and Hollow bluff bodies on the performance and dynamics of flag-based energy harvester. *Sustain. Energy Technol. Assess.* **55**, 102882 (2023).
17. Chen, W., Ji, C., Xu, D., Zhang, Z. & Wei, Y. Flow-induced vibrations of an equilateral triangular Prism at various angles of attack. *J. Fluids Struct.* **97**, 103099 (2020).
18. Lian, J., Yan, X., Liu, F. & Zhang, J. Analysis on flow-induced motion of cylinders with different cross sections and the potential capacity of energy transference from the flow. Shock and Vibration. 1–19 (2017). (2017).
19. Sharma, A. A. & Saha, S. K. Flow-induced vibration of a cylinder subjected to proximity interference by a downstream-cylinder. *J. Fluid Mech.* **1015**, A16 (2025).
20. Sun, H., Yang, Z., Li, J., Ding, H. & Lv, P. Performance evaluation and optimal design for passive turbulence control-based hydrokinetic energy harvester using EWM-based TOPSIS. *Energy* **298**, 131377 (2024).
21. Mujtaba, A. et al. Hydrodynamic energy harvesting analysis of two piezoelectric tandem flags under influence of upstream body's wakes. *Appl. Energy*. **282** (PA), 116173 (2021).
22. Shah, M. M. et al. Experimental investigation of the wake of tandem cylinders using Pivoted flapping mechanism for piezoelectric flag. *Ocean Eng.* **310** (P1), 118587 (2024).
23. Ali, U., Islam, M., Janajreh, I., Fatt, Y. Y. & Alam, M. M. Unveiling the dynamics of 2-DOF flow-induced vibrations and heat transfer: A comprehensive study of multi-cylinder configurations. *Int. Commun. Heat Mass Transfer*. **164**, 108780 (2025).
24. Fan, T., Zhou, S., Sun, H. & Chen, C. Numerical simulation of FIV of PTC-cylinder with nonlinear springs at high Reynolds number. *J. Ship Res.* **17** (3), 160–169 (2022).
25. Lian, J. et al. Hydrokinetic energy harvesting from flow-induced motion of oscillators with different combined sections. *Energy* **269**, 126814 (2023).
26. Liu, F. et al. Experimental investigation on flow-induced rotation of two mechanically tandem-coupled cylinders. *Appl. Sci.* **12** (20), 10604 (2022).
27. Feng, W., Yang, X., Yan, X. & Li, L. Investigation on flow-induced rotation of coupled double cylinders arranged in tandem. Journal of Offshore Mechanics and Arctic Engineering. **2024**, 87851 (2024).
28. Zhang, B., Song, B., Mao, Z., Li, B. & Gu, M. Hydrokinetic energy Harnessing by spring-mounted oscillators in FIM with different cross sections: from triangle to circle. *Energy* **189**, 116249 (2019).
29. Hu, G. et al. Experimental investigation on the efficiency of circular cylinder-based wind energy harvester with different rod-shaped attachments. *Appl. Energy*. **226**, 682–689 (2018).
30. Zhu, H. et al. High performance energy harvesting from flow-induced vibrations in trapezoidal oscillators. *Energy* **236**, 121484 (2021).

31. Ma, C. et al. Hydrokinetic energy conversion from flow-induced motion by two rigidly coupled triangular prisms with variable excitation voltage. *Energy* **322**, 135757 (2025).
32. Tan, J. et al. Study on linear generator applied in tidal energy converter based on flow-induced motion. *Acta Energiae Solaris Sinica.* **41** (09), 9–14 (2020). (in chinese).
33. Zhang, H. et al. Xie, L. A high-output performance disc-shaped liquid-solid triboelectric nanogenerator for harvesting omnidirectional ultra-low-frequency natural vibration energy. *Nano Energy*. **121**, 109243 (2024).
34. Lo, J. C. C., Thompson, M. C., Hourigan & Zhao, J. Order of magnitude increase in power from flow-induced vibrations. *Renew. Sustain. Energy Rev.* **205**, 114843 (2024).
35. Li, Z., Zhao, T., Niu, B., Ma, Y. & Hu, C. A hydrokinetic Turbine-Based Triboelectric-Electromagnetic hybrid generator for ocean current energy harvesting. *Energy. Conv. Manag.* **326**, 119473 (2025).
36. Shao, N., Lian, J., Liu, F., Yan, X. & Li, P. Experimental investigation of flow induced motion and energy conversion for triangular Prism. *Energy* **194**, 116865 (2020).
37. Lian, J. et al. Experimental investigation of Flow-Induced motion and energy conversion for two rigidly coupled triangular prisms arranged in tandem. *Energies* **15**, 8190 (2022).
38. Shao, N., Lian, J., Yan, X., Liu, F. & Wang, X. Experimental study on energy conversion of flow induced motion for two triangular prisms in staggered arrangement. *Energy* **249**, 123764 (2022).

Author contributions
Conceptualization: H.W.; Methodology: H.W. and M.H.; Visualization: H.W.; Funding acquisition: N.S.; Project administration: G.L. and X.S.; Supervision: P.X.; Writing—original draft: H.W.; Writing—review and editing: N.S. All authors have read and agreed to the published version of the manuscript.

Funding
This research was supported by the National Natural Science Foundation of China (Grant No. 52409085); the Hebei Natural Science Foundation (Grant No. E2025402113, No. E2024402142); and the Science and Technology Project of Hebei Education Department (Grant No. BJK2023099).

Declarations

Competing interests
The authors declare no competing interests.

Additional information
Correspondence and requests for materials should be addressed to N.S.

Reprints and permissions information is available at www.nature.com/reprints.

Publisher's note Springer Nature remains neutral with regard to jurisdictional claims in published maps and institutional affiliations.